

## RESEARCH ARTICLE

# Formin 2 regulates the stabilization of filopodial tip adhesions in growth cones and affects neuronal outgrowth and pathfinding *in vivo*

Abhishek Sahasrabudhe, Ketakee Ghate\*, Sampada Mutalik\*, Ajesh Jacob\* and Aurnab Ghose<sup>†</sup>

## ABSTRACT

Growth cone filopodia are actin-based mechanosensory structures that are essential for chemoreception and the generation of contractile forces necessary for directional motility. However, little is known about the influence of filopodial actin structures on substrate adhesion and filopodial contractility. Formin 2 (Fmn2) localizes along filopodial actin bundles and its depletion does not affect filopodia initiation or elongation. However, Fmn2 activity is required for filopodial tip adhesion maturation and the ability of filopodia to generate traction forces. Dysregulation of filopodia in Fmn2-depleted neurons leads to compromised growth cone motility. Additionally, in mouse fibroblasts, Fmn2 regulates ventral stress fiber assembly and affects the stability of focal adhesions. In the developing chick spinal cord, Fmn2 activity is required cell-autonomously for the outgrowth and pathfinding of spinal commissural neurons. Our results reveal an unanticipated function for Fmn2 in neural development. Fmn2 regulates structurally diverse bundled actin structures, parallel filopodial bundles in growth cones and anti-parallel stress fibers in fibroblasts, in turn modulating the stability of substrate adhesions. We propose Fmn2 as a mediator of actin bundle integrity, enabling efficient force transmission to the adhesion sites.

**KEY WORDS:** Formin 2, Growth cone, Filopodia, Substrate adhesion, Spinal commissural interneurons, Axon guidance, Chick, Mouse fibroblast

## INTRODUCTION

Establishment of accurate neuronal connectivity during development is central to nervous system function. Growth cones are dynamic chemosensory structures at the tips of growing axons and dendrites that guide these processes to their synaptic targets. Rod-like, actin-based filopodia on growth cones serve as antennae for guidance cues, which trigger local remodeling of the cytoskeleton to achieve directional motility (Bentley and Toroian-Raymond, 1986; Gomez et al., 2001; Heckman and Plummer, 2013). Additionally, filopodial contractility generates the traction forces necessary for growth cone translocation (Chan and Odde, 2008; Dennerll et al., 1989). Persistent elongation of the filopodia and their ability to generate traction depend on the formation of short-lived, integrin-based point contacts along their length and at the tip. These adhesion sites

act as a molecular clutch, transiently anchoring the rearward actin flow to the integrin receptors engaged with the extracellular matrix (ECM) (Bornschiögl, 2013; Mallavarapu and Mitchison, 1999; Mitchison and Kirschner, 1988). Clutch engagement slows down the retrograde flow, allowing cytoskeletal forces to be transduced onto the substrate as traction. In addition, unbalanced actin polymerization at the tip increases membrane protrusion. Recently, a second mechanism of filopodial force generation has been described involving helical buckling of filopodial actin bundles pulling on the substrate engaged to the filopodial tip (Leijnse et al., 2015). These studies highlight the importance of filopodial tip adhesions, although less is known about the mechanisms underlying adhesion dynamics and force transduction through the filopodial shaft.

In neuronal growth cones, integrins have been shown to cluster at filopodial tips upon induction with NGF (Grabham and Goldberg, 1997). Integrin-dependent signaling, analogous to that seen in non-neuronal cells, has been reported in a few studies (Gomez and Letourneau, 1994; Gomez et al., 1996; Myers and Gomez, 2011) and mechanochemical signaling through focal adhesion kinase (FAK) has been shown to stabilize the early adhesions (Moore et al., 2009, 2012; Robles and Gomez, 2006).

Multiple actin remodeling activities regulating filopodial initiation and elongation have been described (Gupton and Gertler, 2007; Lundquist, 2009; Mattila and Lappalainen, 2008). Several members of the formin family have been implicated in filopodia formation, including the Diaphanous-related formins (Block et al., 2008; Goh and Ahmed, 2012; Schirenbeck et al., 2005), DAAM (Jaiswal et al., 2013) and FMNL2 (Block et al., 2012). In the growth cone, the role of Dia2 (Diaph2) and DAAM has been highlighted (Dent et al., 2007).

Formin 2 (Fmn2) was originally described as enriched in neuronal tissue (Leader and Leder, 2000), but little is known about its function in the nervous system. Recently, mutations in *FMN2* have been associated with human intellectual and cognitive disabilities, and correlated with reduced dendritic spines and synaptic density in mice (Law et al., 2014; Mozhui et al., 2008). Mammalian Fmn2 mediates spindle positioning and meiosis during oocyte development by generating contractile actin networks (Leader et al., 2002; Schuh and Ellenberg, 2008). This activity is conserved in the *Drosophila* ortholog of Fmn2 (Rosales-Nieves et al., 2006).

In this study, we find in chick that Fmn2 regulates growth cone translocation by mediating filopodial mechanotransduction and tip adhesion stabilization. In mouse fibroblasts, Fmn2 maintains focal adhesion stability via an analogous function in the ventral stress fibers. We show that Fmn2 is necessary for pathfinding by spinal commissural neurons, underscoring the importance of Fmn2 in the development of neural circuits.

Indian Institute of Science Education and Research (IISER) Pune, Dr Homi Bhabha Road, Pune 411008, India.

\*These authors contributed equally to this work

<sup>†</sup>Author for correspondence (aurnab@iiserpune.ac.in)

Received 19 August 2015; Accepted 23 December 2015

## RESULTS

### Fmn2 is enriched in the chick spinal cord and localizes to the filopodial actin bundles in neuronal growth cones

We evaluated the differential expression of *Fmn2* mRNA using quantitative real-time PCR (qRT-PCR) in the developing chick embryo. *Fmn2* transcript was enriched in the central nervous system, with the highest expression in the developing spinal cord (Fig. 1A). Monitoring *Fmn2* transcript levels in whole embryos revealed persistent expression through developmental stages HH14 to HH22 (Fig. 1B). This period coincides with the phase of outgrowth and floor plate crossing by the spinal commissural neurons (Yaginuma et al., 1994).

To assess the intracellular distribution of Fmn2 in neurons, we raised a polyclonal antibody against chick Fmn2 (anti-gFmn2). The specificity of the antibody was confirmed by western blot on lysates from control and two independent Fmn2-specific translation-blocking morpholino-transfected spinal cord tissue (Fig. 1C, Fig. S1A,A'). In immunoblots of spinal lysates, anti-gFmn2 antibody detected a single band at the expected size, which was significantly reduced in lysates from embryos electroporated with either of the two Fmn2-specific morpholinos.

As *Fmn2* mRNA showed sustained expression in the developing spinal cord, we analyzed the distribution of endogenous Fmn2 protein by immunofluorescence in spinal neurons from HH26/27 chick embryos cultured on fibronectin-coated cover glass. Fmn2 was seen to preferentially localize to the actin bundles, which extended into the growth cone lamellipodia (Fig. 1D–D", Fig. S1B–C"). Occasionally, Fmn2 was detected at the filopodial tip, perhaps indicative of a role in the formation or elongation of filopodia (Fig. 1D–D"). Growth cones transfected with *Fmn2*-specific morpholinos showed an overall reduction in endogenous Fmn2 protein levels (Fig. 1E–E", Fig. S1D). Additional evidence for antibody specificity came from pre-adsorption of the anti-gFmn2 antibody with the epitope peptide prior to immunofluorescence studies. Peptide pre-adsorption resulted in a strong reduction in the overall staining with no signal detected on filopodial actin bundles (Fig. S1D).

Further, we evaluated the localization of transfected GFP-tagged mouse Fmn2 (mFmn2-GFP) in spinal neurons. To reduce the cytosolic signal resulting from overexpression, growth cones were permeabilized prior to fixation. Similar to the distribution of endogenous chick Fmn2, mFmn2-GFP was detected along actin bundles in filopodia and their extended roots. mFmn2-GFP also localized to the tips of some filopodia (Fig. 1F–F"). By contrast, overexpression of soluble GFP showed a diffuse distribution within the central region of the growth cone and was not enriched in filopodial actin bundles (Fig. S2).

Thus, using two complementary approaches – antibody-based detection of endogenous chick Fmn2 and expression of the mouse ortholog of Fmn2 – we show that Fmn2 preferentially localizes to actin bundles in growth cone filopodia.

### Fmn2 regulates growth cone cytoarchitecture and motility

We analyzed Fmn2 morphant spinal growth cones from HH26/27 chick embryos to evaluate the effect of Fmn2 depletion on growth cone morphology (Fig. 2A,B). The overall growth cone area was reduced in the Fmn2 morphants compared with the control treatment ( $P=0.0019$ ; Fig. 2C).

Formins are known regulators of actin filament nucleation, elongation and bundling (Bor et al., 2012; Chesarone and Goode, 2009; Rosales-Nieves et al., 2006; Schuh, 2011). The *Drosophila* ortholog of Fmn2, Cappuccino, is also reported to have actin nucleating and bundling activities (Vizcarra et al., 2014). In order to

assess actin organization directly in the chick growth cone, we evaluated actin compaction using homoFRET between phalloidin-Alexa 488 molecules labeling F-actin. homoFRET is measured by analyzing the extent of depolarization of the fluorescence emission after excitation with polarized light. Fluorescence anisotropy is used as a measure of fluorescence depolarization (Chan et al., 2011; Ganguly et al., 2011; Iyer et al., 2012; Tramier and Coppey-Moisan, 2008). Anisotropy measurements were performed by collecting the parallel and perpendicular emissions from the phalloidin-stained growth cones. The anisotropy in the system was calculated using standard equations (see Materials and Methods). A compact arrangement of fluorophores results in higher homoFRET and, consequently, reduced anisotropy, whereas higher anisotropy indicates low homoFRET resulting from a less compact organization of fluorophores. Knockdown of Fmn2 resulted in an increase in fluorescence anisotropy compared with controls ( $P=0.014$ ), indicating reduced homoFRET and therefore decreased actin compaction in these growth cones (Fig. 2D–F).

Live imaging revealed impaired growth cone motility in Fmn2 morphants compared with controls (Fig. 2G,G', Movie 1). Fmn2 knockdown reduced growth cone motility speeds ( $P=0.0098$ ) and displacements ( $P=0.0011$ ) in comparison to the controls (Fig. 2H,I). In addition, Fmn2 morphant growth cones covered significantly less distance over time ( $P=0.013$ ; Fig. S1F). The ratio of the displacement to the distance covered by the growth cone was used as a measure of the persistent directionality for a given growth cone. Compared with the controls, Fmn2 morphants showed impaired persistent directional translocation ( $P=0.0006$ ; Fig. 2J).

Taken together, our analysis reveals a function for Fmn2 in organizing the growth cone actin cytoskeleton and in the regulation of growth cone structure and motility.

### Reduction of Fmn2 impairs filopodia dynamics

As Fmn2 localized to actin bundles in the filopodia, we assessed the effects of Fmn2 depletion on filopodia. Both filopodia numbers per growth cone ( $P=0.0022$ ) and filopodial lengths ( $P=0.0011$ ) decreased upon Fmn2 depletion (Fig. 3A,B). Live, time-lapse imaging showed that both the number of filopodia initiation events per growth cone and the elongation rates were unaltered upon Fmn2 knockdown (Fig. 3C,D, Fig. S4). Filopodial persistence was evaluated by measuring filopodial lifetimes. Depletion of Fmn2 resulted in reduced filopodial lifetimes ( $P=0.02$ ) and an increase in the number of short-lived filopodia (Fig. 3E,F).

To validate a role for Fmn2 at the growth cone, we introduced the morpholino-resistant mouse ortholog of Fmn2 in the morphant chick neurons. This successfully rescued the growth cone area, filopodial numbers and filopodial lengths in the Fmn2 morphant growth cones (Fig. 3G–I).

These experiments implicate Fmn2 function in growth cone cytoarchitecture and in filopodia dynamics by influencing filopodial stability.

### Fmn2 depletion impairs substrate attachment

The formation of substrate attachments is central to filopodial stabilization. We tested the ability of growth cones to develop point contacts along the filopodia using autophosphorylation of focal adhesion kinase at Y397 (pFAK) as a readout of integrin-dependent development of substrate attachments. Knockdown of Fmn2 resulted in an overall reduction of the pFAK signal at the growth cone ( $P=0.0031$ ; Fig. S3F,G). The distribution of substrate adhesions was analyzed by pFAK fluorescence intensity line scans along the filopodia. Control morpholino-treated filopodia

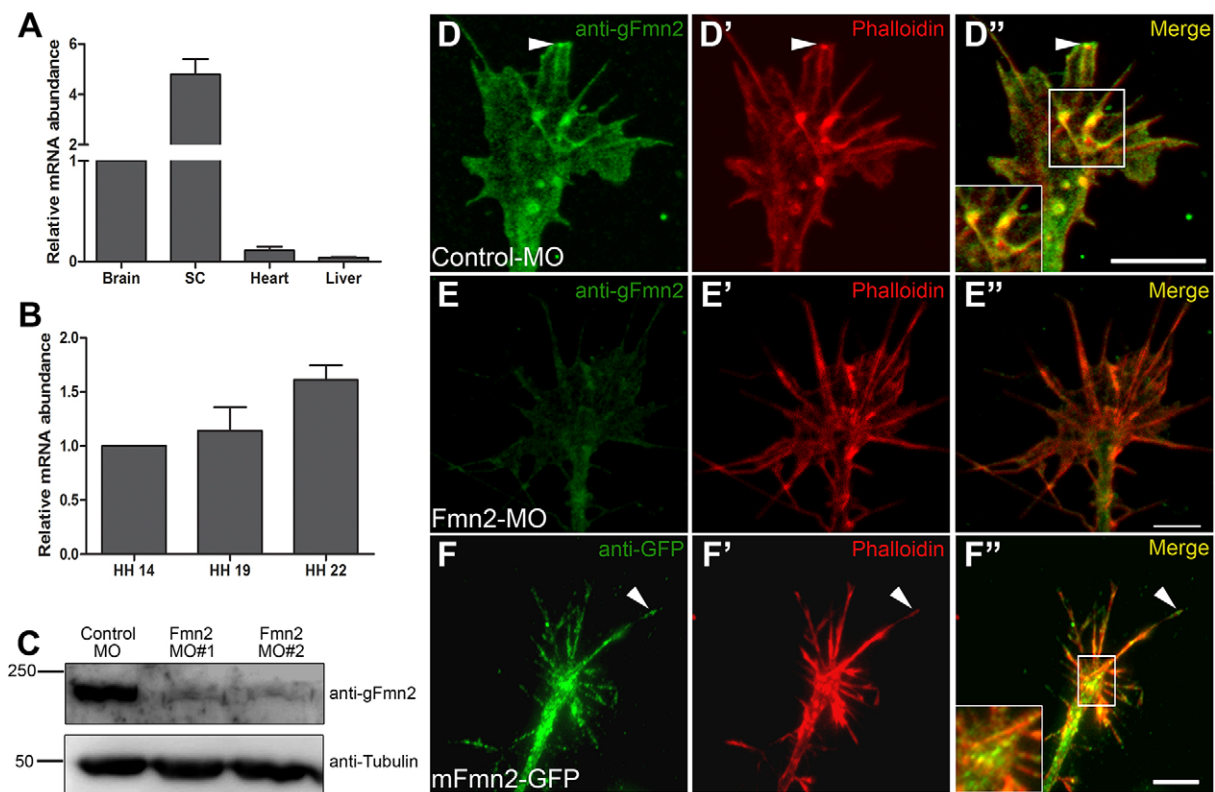


**Fig. 1. Enrichment and distribution of *Fmn2* in the developing nervous system and spinal growth cones.** (A) Relative abundance of *Fmn2* mRNA in different tissues of the stage HH26 chick embryo. *Fmn2* transcript is highly enriched in the spinal cord (SC) compared with other tissues. Data are mean $\pm$ s.e.m. (B) Relative abundance of *Fmn2* transcript in whole embryos across different developmental stages, showing sustained *Fmn2* expression within this developmental window. Data are mean $\pm$ s.e.m. (C) Immunoblot with anti-gFmn2 antibody on lysates from control (Control MO) and two independent *Fmn2* translation-blocking morpholinos (MO#1 and MO#2), showing efficient knockdown of the *Fmn2* protein. The lysates were prepared from the transfected sides of spinal cords 48 h after unilateral *in vivo* electroporation. (D–E'') Representative confocal images of control morpholino-treated (D–D'') and *Fmn2* morpholino-treated (E–E'') spinal growth cones immunostained for endogenous *Fmn2* (anti-gFmn2) and phalloidin to mark the F-actin structures. In the control, *Fmn2* was found to localize to filopodial F-actin bundles, their roots (D'', inset) and at the filopodial tips (arrowhead). In the morphant, the overall signal for anti-gFmn2 was reduced indicating depletion of the *Fmn2* protein. (F–F'') Confocal images of a spinal growth cone transfected with mFmn2-GFP and immunostained for GFP and phalloidin. Similar to endogenous *Fmn2*, mFmn2-GFP localized along filopodial actin bundles, their roots (inset) and at the filopodial tips (arrowhead). Scale bars: 10  $\mu$ m.

showed multiple point contacts along the length, with a distinct pFAK intensity peak at the distal tip (Fig. 4A' inset, C). However, *Fmn2* morphant filopodia lacked this tip accumulation (Fig. 4B' inset, C). In order to directly compare pFAK distribution across control and *Fmn2* knockdown filopodia, which have intrinsic length differences, we normalized the pFAK signal in the distal segment of the filopodia to the total pFAK signal in the filopodia (distal and proximal segments). This analysis revealed that *Fmn2* depletion resulted in a considerable decrease in the pFAK signal from the distal segment of the filopodia ( $P=0.02$ ; Fig. 4D). These data reveal *Fmn2* function in influencing filopodial dynamics via stabilization of tip adhesions.

#### ***Fmn2* depletion impairs traction generation by the filopodial tips**

The importance of tip adhesions has been highlighted in recent studies on filopodial traction forces (Bornschlögl et al., 2013; Chan and Odde, 2008; Hoffmann and Schäfer, 2010; Romero et al., 2013). Our observation of reduced pFAK signal in *Fmn2* morphant filopodial tips prompted us to investigate filopodial traction. Growth cones were cultured on compliant gels embedded with fluorescent beads (Fig. 5A, Movie 2), and the displacement of individual beads at the filopodial tips (Fig. 5A'–A'') was used as an indirect measure of forces exerted by the filopodia on the substrate (Chan and Odde,

2008). *Fmn2* knockdown resulted in a reduced ability to generate traction on the underlying substrate, as seen by the smaller displacement of the beads in comparison to the control filopodia ( $P<0.001$ ; Fig. 5C). Although the frequency of pulling by individual filopodia did not differ significantly (Fig. 5B), the velocity of the pulling events was attenuated upon *Fmn2* depletion ( $P<0.001$ ; Fig. 5D). These data implicate filopodial *Fmn2* activity as being necessary for point contact stabilization and the generation of traction on the substrate.

#### ***Fmn2* regulates focal adhesion stability in fibroblasts**

Our data from chick neuronal filopodia prompted us to investigate whether *Fmn2* has a conserved function in stabilizing focal adhesions (FAs) in fibroblasts. qRT-PCR analysis suggested that siRNA treatment could deplete the endogenous *Fmn2* transcript in mouse NIH3T3 fibroblasts (Fig. S5A). Consistent with our observation in chick growth cones, depletion of *Fmn2* reduced the pFAK (Y397) intensity at the FAs ( $P=0.0047$ ; Fig. S5B).

We monitored paxillin-labeled FAs using live total internal reflection fluorescence (TIRF) microscopy to evaluate the effect of *Fmn2* knockdown on FA dynamics in NIH3T3 cells (Fig. 6A,B). FA parameters were extracted using an automated image analysis platform (Berginski et al., 2011). Compared with the control cells, the *Fmn2* siRNA-treated cells showed reduced FA size ( $P<0.0001$ ),

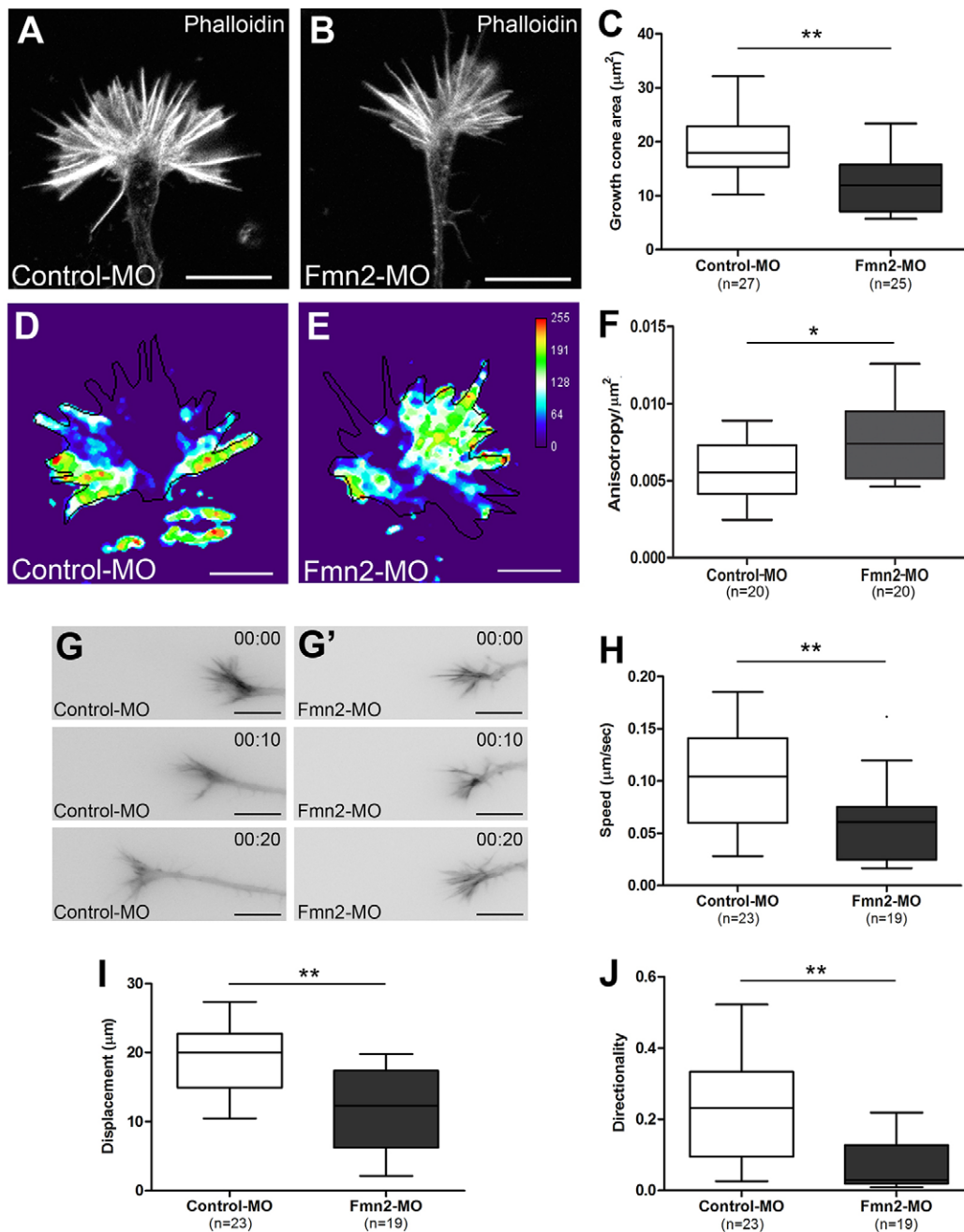


**Fig. 2. Effect of Fmn2 depletion on growth cone morphology, actin organization and motility.** (A,B) Representative images of control morpholino-treated and Fmn2 morpholino-treated spinal growth cones labeled with phalloidin. (C) Knockdown of Fmn2 reduced the growth cone area in comparison to control treatments. (D,E) Representative heat maps for fluorescence anisotropy signals as a measure of homoFRET between phalloidin-Alexa 488 molecules. The black outline marks the edge of the growth cones. The heat map calibration bar in E shows the color code corresponding to an 8-bit image. (F) Knockdown of Fmn2 increased fluorescence anisotropy as a result of reduced phalloidin-Alexa 488 homoFRET. This indicates impaired actin compaction in the Fmn2-depleted growth cones compared with control morpholino-treated growth cones. (G,G') Representative frames from time-lapse imaging for control and Fmn2 morphant growth cones. The time stamp shows minutes elapsed. (H) Comparison of translocation speeds showing that Fmn2 morphant growth cones migrate considerably more slowly than control growth cones. (I) Displacement from the initial position was less in Fmn2 morphant growth cones than in controls. (J) Knockdown of Fmn2 reduced the directionality of translocating growth cones. The ratio of growth cone displacement to the total accumulated distance covered was used to estimate persistent directionality. Data are represented as box and whisker plots using the Tukey method. The horizontal line inside the box represents the median. \* $P < 0.05$ , \*\* $P < 0.01$ ; Mann-Whitney test. Scale bars: 10  $\mu\text{m}$ .

although the number of FAs per cell was not altered significantly (Fig. 6C,D). Further analysis revealed that although Fmn2-deficient cells showed comparable FA assembly rates, they disassembled more quickly ( $P=0.0002$ ; Fig. 6E,G). In addition, the duration of the disassembly phase was increased ( $P < 0.0001$ ; Fig. 6H) and the

assembly phase was reduced following Fmn2 knockdown ( $P=0.0071$ ; Fig. 6F).

Taken together, these data show that FAs in Fmn2-depleted cells show increased disassembly and are consequently unstable and smaller.

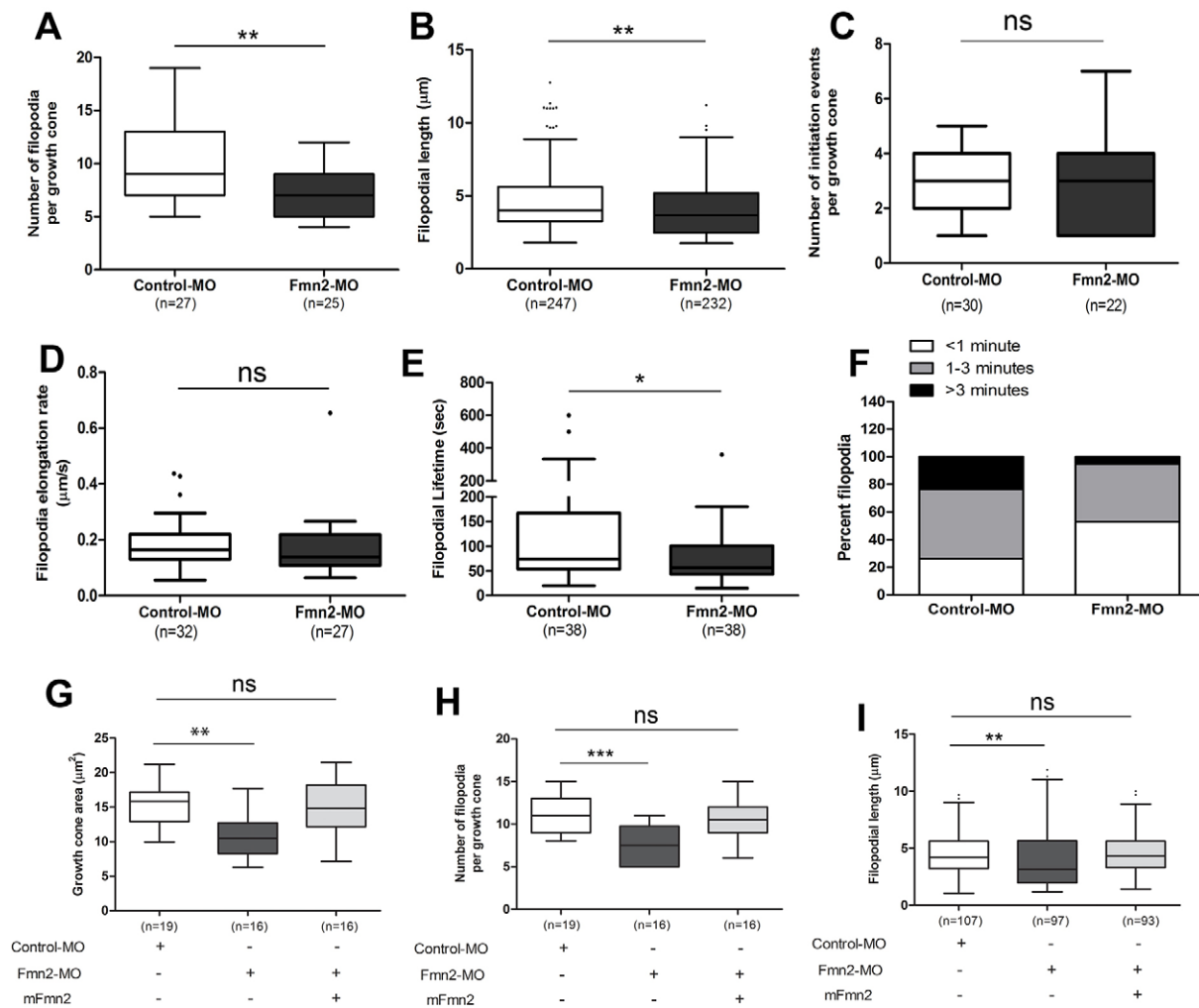


**Fig. 3. Fmn2 knockdown affects growth cone filopodial dynamics and tip adhesion.** (A) The number of filopodia per growth cone was reduced following Fmn2 knockdown. (B) The average length of filopodia was shorter upon Fmn2 knockdown. (C,D) Fmn2 depletion did not affect the number of filopodia initiation events or filopodial elongation rates. (E) Filopodial lifetimes were shorter in Fmn2 morphant growth cones than in control morpholino-treated growth cones. (F) Percentage of filopodia binned in different groups based of their lifetimes. The short-lived filopodia, lasting less than 1 min, increased upon Fmn2 depletion. Conversely, the population of long-lived filopodia with lifetimes of more than 3 min was reduced in Fmn2 morphant growth cones. (G-I) Introduction of the morpholino-resistant mouse ortholog of Fmn2 (mFmn2) restored growth cone area, filopodial number and filopodial length so that they were comparable to control morpholino-treated growth cones. Data are represented as box and whisker plots using the Tukey method with the exception of F. The horizontal line inside the box represents the median. Statistical comparisons for A-E were performed using the Mann-Whitney test; the Kruskal-Wallis test followed by Dunn's post-test was employed for G-I; \* $P \leq 0.05$ , \*\* $P \leq 0.01$ , \*\*\* $P \leq 0.001$ ; ns, non-significant.

### Fmn2 mediates actin turnover in ventral stress fibers

Expression of mFmn2-GFP in NIH3T3 cells showed a heterogeneous distribution. mFmn2-GFP was localized to irregularly shaped, often fibrillar structures closely apposed to the ventral surface (Fig. 7A,B). Typically, these structures were subnuclear and perinuclear and were largely devoid of actin. Interestingly, Fmn2 was also found to localize along ventral actin stress fibers that span two FAs (Fig. 7D-F'). The Fmn2-labeled ventral stress fibers were not only perinuclear, forming a cage-like network at the base of the nucleus, but also extended towards the periphery. Fmn2 was unevenly distributed along the length of these ventral stress fibers (Fig. 7D-H). Fmn2 on stress fibers was restricted to the juxta-FA actin bundle but was largely undetected in the central region of the paxillin-labeled FAs (Fig. 7C).

To test if Fmn2 activity influences actin dynamics at the ventral stress fibers, we employed fluorescence recovery after photobleaching (FRAP) analysis on NIH3T3 cells co-transfected

with siRNAs and mGFP-Actin (Fig. 7I). Analysis of the FRAP curves revealed longer recovery times ( $P < 0.0001$ ) in Fmn2-deficient cells (fast  $t_{1/2} = 55.84 \pm 8.49$  s; slow  $t_{1/2} = 4.25 \pm 3.27$  s) compared with the control cells (fast  $t_{1/2} = 80.68 \pm 26.21$  s; slow  $t_{1/2} = 8.47 \pm 5.04$  s). This suggests that Fmn2 activity is required for efficient actin monomer exchange in the ventral stress fibers. Mechanotransduction along stress fibers has been reported to influence FA stability (Burridge and Wittchen, 2013; Oakes et al., 2012; Walcott and Sun, 2010) and the defects in FA dynamics observed upon Fmn2 knockdown are likely to be a consequence of impaired ventral stress fiber assembly.

### Fmn2 is required for midline crossing by spinal commissural neurons

As our *in vitro* data implicated Fmn2 function in growth cone dynamics of spinal neurons, we investigated its *in vivo* relevance by depleting Fmn2 from developing chick spinal cords. Midline crossing of spinal commissural interneurons was evaluated

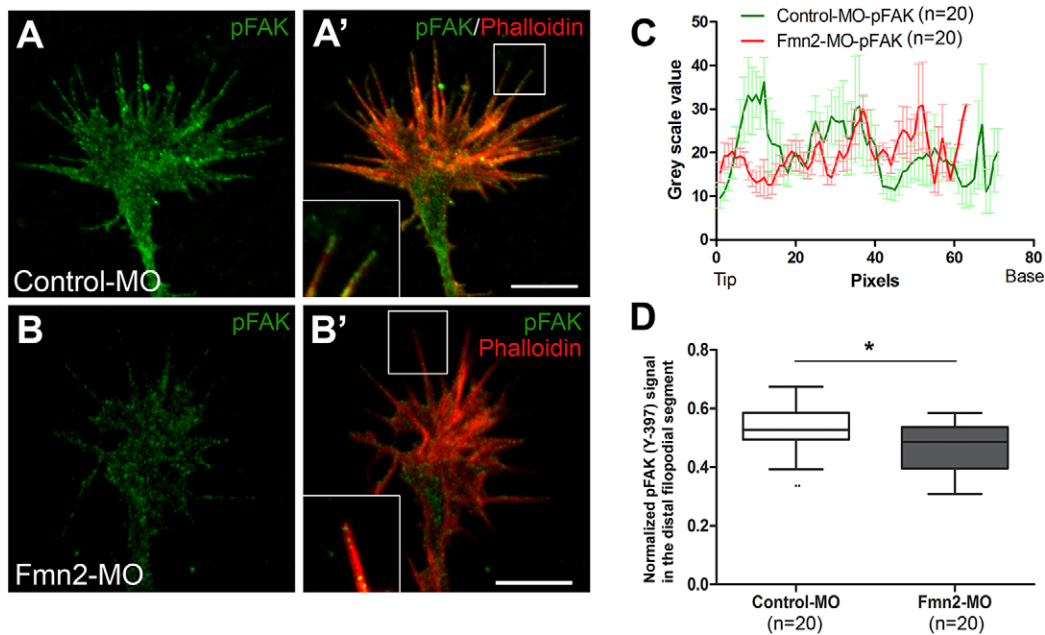


**Fig. 4. Fmn2 depletion alters the growth cone-substrate interaction.** (A–B') Representative micrographs of control morpholino-treated (A,A') or Fmn2 morpholino-treated (B,B') growth cone immunostained for pFAK (Y-397) and phalloidin. The pFAK signal seen at filopodial tips in the control is lost in the Fmn2 morphant (insets). (C) pFAK signal from line traces along the filopodia. The marked increase in pFAK signal at the filopodial tip in control growth cones is absent in Fmn2 morphant growth cones. The line represents the mean and error bars indicate s.e.m. (D) Normalized pFAK signal in the distal segments of filopodia. A reduction is seen for the pFAK signal in the distal segment of the Fmn2 morphant filopodia as compared with the distal halves of the control filopodia. Data are represented as box and whisker plots using the Tukey method. The horizontal line inside the box represents the median. \* $P < 0.05$ ; Mann–Whitney test. Scale bars: 10  $\mu\text{m}$ .

following *in ovo* electroporation of control and Fmn2 translation-blocking morpholinos.

Outgrowth and floor plate crossing of spinal commissural neurons occurs between HH19 and HH26 (Yaginuma et al., 1994). Initial experiments involved unilateral *in ovo* electroporation of morpholinos at HH14 followed by immunostaining of HH26 cryosections with axonin 1 antibodies. Axonin 1 is expressed on the axons of pre-crossing spinal commissurals but its expression disappears following

floor plate crossing (Baeriswyl and Stoeckli, 2008; Fitzli et al., 2000; Stoeckli and Landmesser, 1995). At HH26, no axonin 1 signal was detected in the spinal cords of control morpholino-treated embryos. However, all stage-matched Fmn2 morphant embryos showed sustained axonin 1 staining only in the electroporated half of the spinal cord (Fig. S6A–D'; three embryos in each group).

Encouraged by these results we investigated the role of Fmn2 in spinal circuit development by evaluating the Atoh1-expressing d11

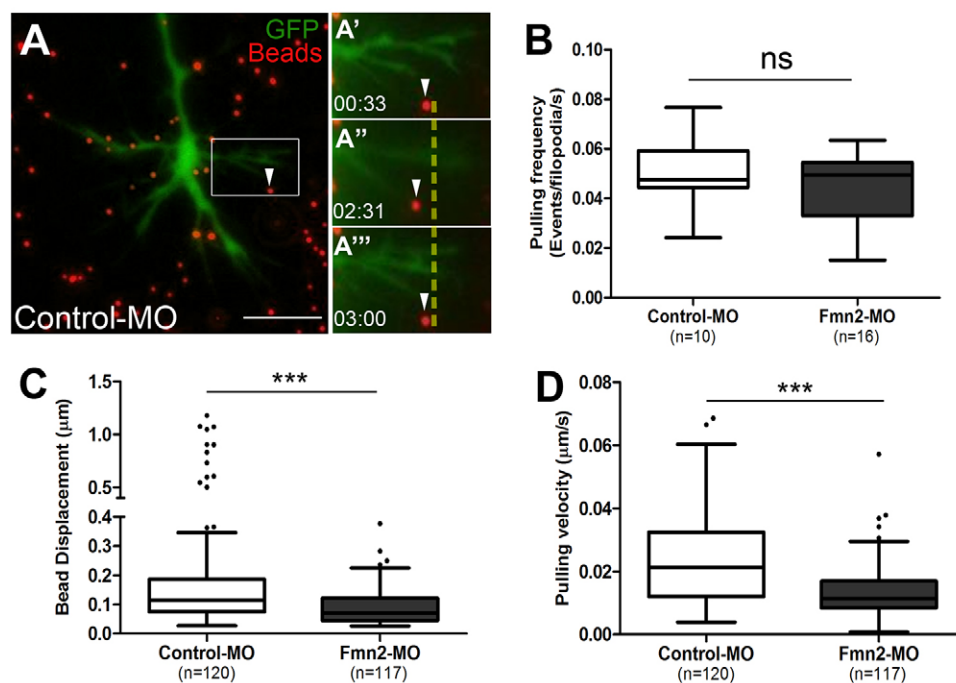


**Fig. 5. Fmn2 activity is necessary for the generation of filopodial traction forces.**

(A) Representative micrograph of a control morpholino- and GFP-transfected growth cone plated on polyacrylamide gel with embedded fluorescent beads. The movement of a bead (arrowhead) close to the filopodium tip is tracked over time to assess the traction force exerted by the filopodium on the compliant substrate. (A'–A''') Representative frames from a time-lapse sequence for the region boxed in A. The time stamp shows minutes: seconds elapsed. (B) No difference was observed in the number of pulling events between control and Fmn2 morphant growth cone filopodia. (C) Fmn2 depletion attenuates bead displacement during individual pulling events. (D) The velocity of pulling events is reduced after Fmn2 depletion, indicating a reduced ability to generate traction forces. Data are represented as box and whisker plots using the Tukey method. The horizontal line inside the box represents the median. \*\*\* $P < 0.001$ ; ns, non-significant; Mann–Whitney test. Scale bar: 10  $\mu\text{m}$ .

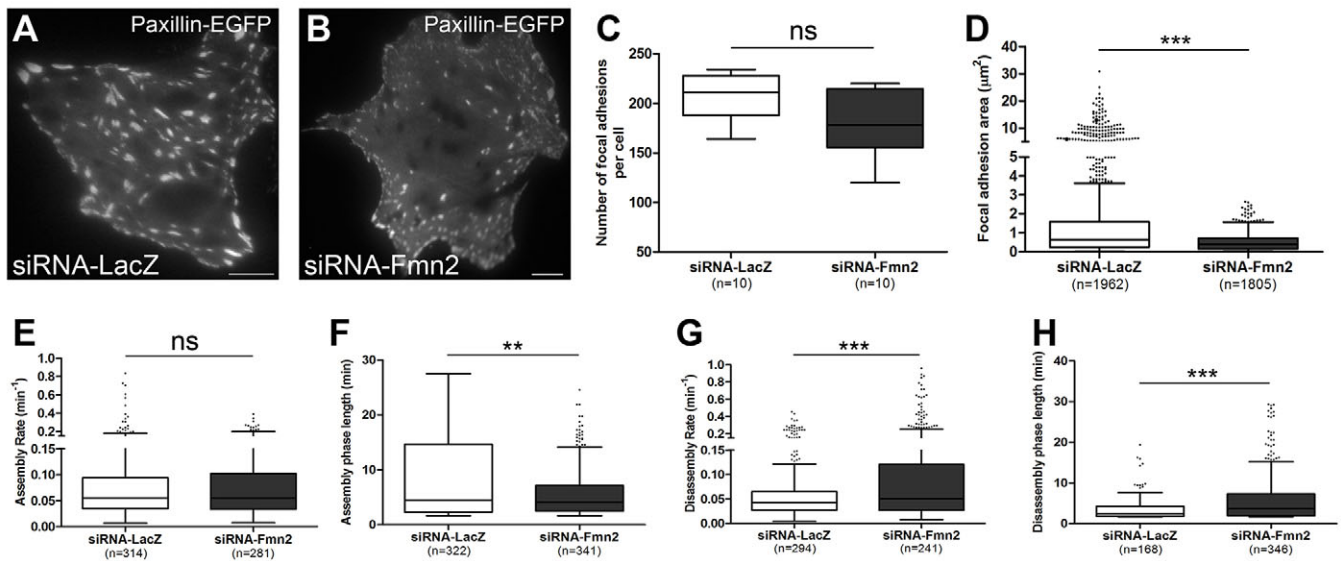


**Fig. 6. Fmn2 is required for focal adhesion stability.** (A,B) Representative TIRF images for Fmn2 siRNA-treated mouse NIH3T3 fibroblasts co-transfected with paxillin-EGFP. (C) Fmn2 knockdown had no effect on the number of focal adhesions (FAs) per cell. (D) A marked reduction in FA size was observed in the Fmn2-depleted cells as compared with control cells. (E) FA assembly rate was unaltered after Fmn2 knockdown. (F) Assembly phase length for FAs was reduced upon Fmn2 depletion. (G) Fmn2 knockdown resulted in an increase in FA disassembly rates as compared with the control cells. (H) The FA disassembly phase length was increased following Fmn2 depletion. Data are represented as box and whisker plots using the Tukey method. The horizontal line inside the box represents the median. \*\* $P < 0.01$ , \*\*\* $P < 0.001$ ; ns, non-significant; Mann–Whitney test. Scale bars: 10 µm.

subpopulation of spinal commissural interneurons. Morpholinos were unilaterally co-electroporated along with Atoh1-tau-mCherry at HH14 and stage-matched spinal cords were analyzed in open-book preparations at HH26 to visualize the dII commissural neurons. In control embryos, the majority of the commissural neurons had crossed the floor plate and taken a rostral turn along a stereotyped sigmoidal trajectory (Fig. 8A-A’). However, the Fmn2 morphant embryos showed compromised midline crossing, with many dII tracts stalling at the floor plate (Fig. 8B-B’). This analysis showed that depletion of Fmn2 reduces the ability of the commissural neurons to efficiently cross the floor plate as compared with the control morpholino-treated embryos (Fig. 8D,E). We further analyzed the contralateral sigmoidal trajectories. Compared with control embryos, Fmn2 morphants showed a reduction in the proportion of post-crossing axonal tracts displaying the stereotyped sigmoidal trajectory (Fig. 8F). To test for a cell-autonomous requirement for Fmn2 in dII neuron pathfinding, we expressed the mouse ortholog of Fmn2 specifically in these commissural neurons using the *Atoh1* enhancer (Atoh1-mFmn2). The chick-specific morpholino used to deplete endogenous Fmn2 had no binding sites on the mouse *Fmn2* cDNA. Co-electroporation of Atoh1-mFmn2 and control morpholino had no discernible effect on the dII neurons. However, expression of Atoh1-mFmn2 in dII neurons rescued both the midline crossing and contralateral trajectory phenotypes of the Fmn2 morphants (Fig. 8C-F).

Taken together, our analysis highlights the cell-autonomous requirement of Fmn2 in the development of dII spinal commissural neuron circuits and emphasizes the evolutionary conservation of Fmn2 function in avian and mammalian lineages.

## DISCUSSION

Filopodia are central to the establishment of neuronal circuits during development. A number of proteins have been identified in recent years, including members of the formin family, as being necessary for the initiation and elongation of filopodia. However, less is

known about activities that regulate the stability and maturation of the filopodial tip adhesions and, in turn, the generation of traction forces. We identify the Rho-independent formin Fmn2 as a crucial regulator of filopodial adhesion dynamics and growth cone motility. Fmn2 function *in vivo* was tested in chick dII spinal commissural neurons and was found to be necessary for outgrowth and pathfinding.

Fmn2 localized to filopodial actin bundles in spinal neurons. Knockdown of Fmn2 reduced the number and length of filopodia. Unlike other formins (Block et al., 2008; Goh and Ahmed, 2012; Mellor, 2010), Fmn2 depletion did not affect filopodial elongation rates or the number of initiation events. However, filopodial lifetimes were severely reduced, suggesting compromised filopodial stability. Although it is possible that *Fmn2* null neurons may reveal defects in filopodia initiation and elongation not observed in transient knockdowns, our results support a dominant and novel function for Fmn2 in filopodial stabilization via tip adhesions.

The persistence of protrusive structures and their function in motility depend on the formation of stable substrate attachments. FAK autophosphorylation at Y397 is central to assembly and mechanotransduction at integrin-based adhesion sites. In growth cones, FAK activity mediates filopodial dynamics, development of adhesions and traction forces and pathfinding (Chacón et al., 2012; Moore et al., 2012; Robles and Gomez, 2006). Fmn2 depletion reduced pFAK (Y397) at the filopodia tips, suggesting impaired adhesive stability, in concurrence with the decreased filopodial lifetimes observed.

Filopodial tip adhesions regulate filopodial contractility and the generation of traction forces (Moore et al., 2009, 2012; Romero et al., 2013). We find that Fmn2-depleted filopodia are severely compromised in their ability to generate traction forces, possibly owing to impaired engagement of the cytoskeleton with the ECM. Collectively, these data agree with the growth cone translocation defects observed in Fmn2 morphant neurons.

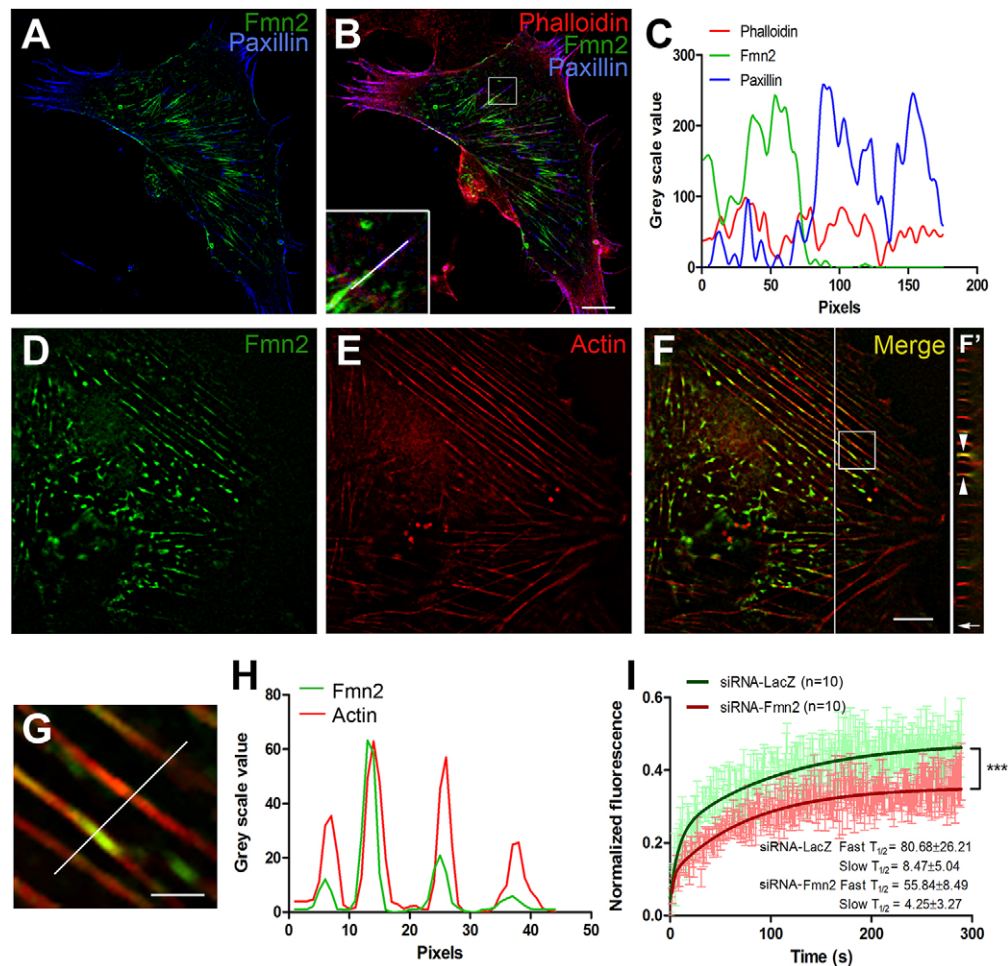


**Fig. 7. Fmn2 localizes to actin stress fibers and is involved in stress fiber assembly.** (A) Representative confocal micrograph showing the distribution of Fmn2 along with the FA marker paxillin in fixed NIH3T3 fibroblasts. (B) Representative confocal micrograph showing the distribution of Fmn2 along with the FA marker paxillin and F-actin marked by phalloidin in fixed cells. Inset shows a magnified view of the boxed region. (C) Line traces showing the fluorescence intensities of phalloidin, Fmn2 and paxillin along the line in the inset in B. Fmn2 is localized at juxta-FA locations on stress fibers but does not extend to the central region of the paxillin-labeled FA. (D,E) Maximum intensity projections of wide-field deconvolved z-stack for the Fmn2 (mFmn2-GFP) and actin (Actin-mRFP) distribution in live NIH3T3 fibroblasts. (F) Merge of D and E showing Fmn2 distribution along ventral stress fibers. (F') y-z projection of the deconvolved stack along the vertical line in F. Arrowheads mark Fmn2 colocalization with ventral stress fibers. Ventral is to the left, as indicated by the arrow. (G) Magnified view of the boxed region in F. (H) Line traces showing the fluorescence intensities for phalloidin and Fmn2 along the line in G. The intensity peaks for Fmn2 and actin coincide indicating colocalization. (I) FRAP curves for mGFP-Actin on ventral stress fibers following siRNA treatment. Depletion of Fmn2 reduced the actin monomer recovery as compared with control siRNA-treated cells. The curve fitting was performed using a double exponential fit and the  $t_{1/2}$  values are represented in seconds  $\pm$  s.e.m. Curve fits were compared using the extra sum-of-squares *F*-test; \*\*\* $P \leq 0.001$ . Scale bars: 10  $\mu$ m in B,F; 2  $\mu$ m in G.

Forces originating from F-actin retrograde flow are transduced onto the substrate by dynamic molecular clutches that link the actin to the extracellular substrate (Bornschlögl et al., 2013; Chan and Odde, 2008; Mallavarapu and Mitchison, 1999). Additionally, helical buckling-induced shortening of the filopodial actin shaft can also contribute to filopodial traction (Leijnse et al., 2015). We propose that Fmn2 knockdown results in disorganized actin bundles in filopodia, impairing its ability to transduce forces to the tip adhesions (Fig. 8G). Reduced actin compaction in Fmn2-depleted growth cones provides early evidence for such a function. Several formins, including Fmn2 and its fly ortholog, have been suggested to have actin bundling functions (Bohnert et al., 2013; Esue et al., 2008; Harris et al., 2006; Machaidze et al., 2010; Schönichen et al., 2013; Vizcarra et al., 2014). Thus, it seems feasible that Fmn2 maintains the structural integrity of filopodial actin bundles, in turn influencing the efficiency of clutch engagement and force transduction.

Anti-parallel acto-myosin stress fibers transduce mechanical forces between the cytoskeleton network and FAs in non-neuronal cells. We found that Fmn2 regulates ventral stress fiber turnover and FA disassembly. Stress fiber dynamics is known to influence FA stability (Burrige and Wittchen, 2013; Chang and Kumar, 2013; Colombelli et al., 2009; Oakes et al., 2012) and these observations are therefore analogous and supportive of our conclusions regarding Fmn2 function in growth cone filopodia. Fmn2 is detected in the myosin-dependent FA proteome (Kuo et al., 2011), and its juxta-FA localization might suggest a function in coupling actin bundles to the adhesion complex, as proposed for INF2 (Skau et al., 2015). Additionally, the cage-like organization of Fmn2 stress fibers around the nucleus might suggest a role in nuclear positioning.

Fmn2 was found to be necessary for commissural neuron outgrowth and pathfinding. This function appears to be conserved across mammalian and avian lineages. Stalling of dII axons at the floor plate and aberrant axonin 1 expression upon Fmn2 depletion

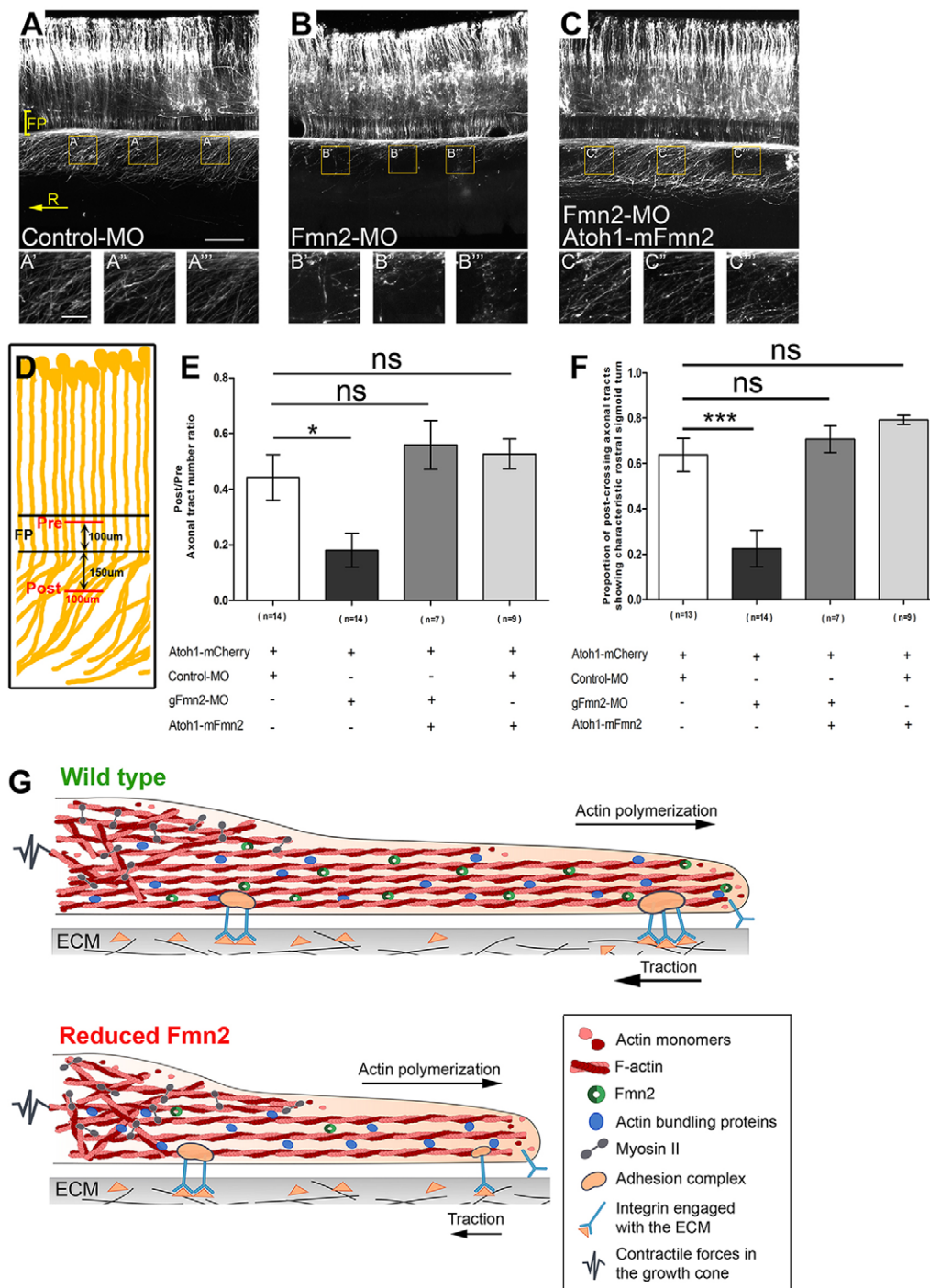


**Fig. 8. Spinal commissural neurons require Fmn2 for midline crossing *in vivo*.** Representative maximum intensity projections of tiled z-stacks of spinal cord open-book preparations (at stage HH26) unilaterally electroporated with Atoh1-tau-mCherry and the indicated morpholino. The electroporated side is at the top and rostral (R) is to the left in each micrograph. FP, floorplate. (A-A'') Control morpholino-treated spinal cords show midline crossing by the Atoh1-positive commissural neurons with most post-crossing tracts taking a stereotyped sigmoidal trajectory towards the rostral direction. (B-B'') Fmn2 morphant spinal cords showed reduced midline crossing and defective post-crossing trajectories. (C-C'') Defects in floor plate crossing and post-crossing trajectories in the Fmn2 morphant commissural neurons were rescued by expressing the morpholino-resistant mouse ortholog of Fmn2 in the Atoh1-positive commissural neurons. (D) Schematic representation of a unilaterally electroporated spinal cord open-book preparation indicating the position of ROIs used to score the number of pre- and post-crossing tracts. FP, floorplate; Pre, ROI position to score pre-crossing tracts; Post, ROI position to score post-crossing tracts. (E) Midline crossing efficiency of the commissural neurons quantified using the ratio of pre-crossing axon tracts to post-crossing axon tracts. This ratio was significantly reduced following Fmn2 morpholino treatment and could be rescued by introducing the mouse ortholog of Fmn2 in the Atoh1-positive commissural neurons. (F) The proportion of post-crossing axonal tracts showing a characteristic sigmoidal trajectory was reduced in Fmn2 morphant spinal cords and could be rescued by expressing mouse Fmn2 in the Atoh1-positive commissural neurons. (G) Model for Fmn2-mediated filopodial stabilization of ROIs used to score the number of pre- and post-crossing tracts. Fmn2 activity maintains optimal actin compaction facilitating force transduction to filopodial tip adhesions. This mechanical feedback is essential for tip adhesion stability and filopodial traction. Data are represented as columns with s.e.m. \* $P \leq 0.05$ , \*\*\* $P \leq 0.001$ ; ns, non significant; one-way ANOVA followed by Dunnett's post-test. Scale bars: 200  $\mu\text{m}$  in A-C; 50  $\mu\text{m}$  in A'-C''.

are consistent with growth cone translocation deficits identified in this study and may represent a delay in axonal outgrowth. The defects in the contralateral side could be an indirect consequence of the delayed arrival of growth cones at the relevant choice points. An additional, independent function of Fmn2 in guidance cue-dependent directional motility is also possible, but elucidation of this role will require an understanding of the upstream regulation of Fmn2 activity.

Our study investigated Fmn2 function in a specific spinal subpopulation, and it remains to be tested whether Fmn2 is a regulator of growth cone dynamics in actively extending neurons in general. In fact, our observation of Fmn2 function in ventral stress fibers and associated FAs in fibroblasts might suggest a broader role in cellular morphogenesis and motility that is not limited to neurons.

Recently, mutations in *Fmn2* have been associated with human intellectual disabilities and with defective fear conditioning and reduced dendritic spine density in mice (Law et al., 2014; Mozhui et al., 2008; Peleg et al., 2010). *Fmn2* mutations are also associated with increased metastatic potential (Charfi et al., 2011; Lynch et al., 2013). The actin organizing and adhesion stabilization functions of Fmn2 identified in our study are likely to offer mechanistic insights to these observations.

This study is the first to characterize Fmn2 function in neurons and identifies an unexpected role in stabilizing adhesive structures via actin bundle assembly, disruption of which leads to impaired development of spinal circuits. Together, these findings highlight the conserved role of Fmn2 in neuronal development and provide a novel mechanistic framework for formin function in cell motility.

## MATERIALS AND METHODS

### *In ovo* injections and electroporations

Freshly fertilized, White Leghorn eggs were procured from Dr BV Rao Institute of Poultry Management and Technology, Pune, India. All animal protocols were in accordance with the procedures approved by the Institutional Animal Ethics Committee, IISER Pune, India. Embryos at stage HH14 were used for electroporation. Spinal cord electroporations were performed similarly to Baeriswyl et al. (2008). See the supplementary Materials and Methods for electroporation details.

Two translation-blocking morpholino sequences were tested (5'-3'): Fmn2 MO#1, CACGGTTTTTATTGCCTGCATTGCA; and Fmn2 MO#2, CCATCTTGATTCCCCATGATTTTC. Standard control morpholino CCTCTTACCTCAGTTACAATTTATA was used as a negative control. Atoh1-tau-mCherry was a generous gift from Prof. Jane Johnson (UT Southwestern Medical Center). The original clone for mouse Fmn2 was obtained from Prof. Philip Leder (Harvard Medical School). See the supplementary Materials and Methods for construction of Atoh1-mFmn2 and pCAG-mFmn2-GFP.

### qRT-PCR for chick embryos and mouse NIH3T3 cells

Tissues were pooled from three chick embryos and a standard total RNA isolation procedure was followed using Trizol (Invitrogen). cDNA was prepared using 2 µg total RNA, oligo-dT (18mer) and M-MLV reverse transcriptase (Promega) according to the manufacturer's recommendations. For whole-embryo qRT-PCR analysis, RNA from three chick embryos was pooled. Each sample had three technical replicates and each experiment was repeated three times. The pooled data were used for statistical analysis and graphical representations. *Fmn2* mRNA was normalized to β-actin and represented using brain expression as the reference.

Primers used (forward and reverse): Fmn2, TCAGCAGCGGATTCTG-AGGCTAAA and ATGCAAGTCCTTGACTGGCTGA; β-actin, AG-ACATCAGGGTGTGATGGTTGGT and TCCAGTTGGTGACAATAC-CGTGT. For qRT-PCR analysis of NIH3T3 cells, including sequences of mouse Fmn2 and β-actin primers, see the supplementary Materials and Methods.

### Antibody generation

A unique peptide sequence for chick Fmn2 (CRQKKGKSLYNIRPK) was selected for antibody generation in rabbits. The peptide was synthesized and injected into rabbit for antibody generation. Antisera (anti-gFmn2) were collected periodically after booster doses and the antibody titer was estimated by ELISA. See the supplementary Materials and Methods for antibody validation.

### Transfection, culture, immunostaining and imaging of primary neurons

Spinal cords from HH26/27 chick embryos were dissected in PBS and trypsinized using 0.05% trypsin, 0.48 mM EDTA (Gibco). The cell suspension was transferred to an electroporation cuvette with appropriate plasmid and morpholino combinations; 10 µg plasmid and 100 µM morpholino were used for transfections. A NEPA21 type II square wave electroporator (Nepagene) was used. Typical transfection efficiency in these experiments was in the range 25-30%. Post-electroporation immunostaining, imaging and quantification of signal, including the analysis of pFAK along filopodia, were undertaken using standard procedures as detailed in the supplementary Materials and Methods.

### Live imaging of neuronal growth cones and evaluation of filopodial traction

Twenty-four hours after electroporation and culturing, the culture medium was replaced with fresh medium. The samples were imaged using a PlanApoN 60×/1.49 objective on an Olympus IX81 system equipped with a Hamamatsu ORCA-R2 CCD camera. Images were captured every 10 s for up to 30 min. The system was equipped with a focus drift correction mechanism and the entire imaging setup was maintained at 37°C without CO<sub>2</sub> during the entire imaging procedure. See the supplementary Materials and Methods for details.

Filopodial traction force assays were modified from an earlier protocol (Chan and Odde, 2008), as detailed in the supplementary Materials and Methods.

### NIH3T3 fibroblast culture and transfections

NIH3T3 fibroblasts were obtained from Dr N. Balasubramanian (IISER Pune) and were tested for contamination prior to use. The cells were maintained using standard culturing procedures in DMEM plus 10% heat-inactivated FBS, 1× Pen Strep (Gibco) and 1× L-glutamine (Gibco, 2 mM). Approximately 2×10<sup>4</sup> cells were seeded in 50 ng/ml fibronectin-coated 4-well cover glass-bottom Nunc Lab-Tek chambers and allowed to attach overnight. siRNA (*lacZ* sense strand, 5'-CGUCGACGGAAUACUUCG-AUU-3'; *Fmn2* sense strand, 5'-UGGUUAGACUUGUGGGUAAUU-3'), paxillin-EGFP (a gift from Rick Horwitz, University of Virginia; Addgene plasmid #15233), paxillin-mCherry (a gift from Martin Schwartz, Yale University), Actin-mRFP (a gift from Bidisha Sinha, IISER Kolkata) and mGFP-Actin (a gift from Ryohei Yasuda, Max Planck Florida Institute of Neuroscience; Addgene plasmid #21948) were transfected using Lipofectamine 2000 according to the manufacturer's protocol (Invitrogen). The cells were incubated for 24 h before imaging.

### TIRF imaging and analysis of FAs in NIH3T3 cells

Twenty-four hours post siRNA plus paxillin-EGFP transfections, the culture medium was replaced with cell imaging medium (L-15 plus 10% heat-inactivated FBS, 1× Pen Strep, 2 mM L-glutamine). The cells were imaged in TIRF mode using an ApoN/TIRF 60×/1.49 objective on an Olympus IX81 system equipped with a Hamamatsu ORCA-R2 CCD camera and the Olympus Cell TIRF module. Images were acquired every 10 s for 30 min. The system was equipped with focus drift correction and the entire imaging setup was maintained at 37°C without CO<sub>2</sub> during the entire imaging procedure. See the supplementary Materials and Methods for details. FAs from ten cells in each treatment representing three biological replicates were used for graphical representation and statistical analysis.

### Imaging NIH3T3 fibroblasts and FRAP analysis on stress fibers

Post-transfection, the cells were fixed and stained with 20 units of phalloidin (Invitrogen) or live imaged using standard protocols. Twenty-four hours

post siRNA plus mGFP-Actin transfection, ventral stress fibers of NIH3T3 cells were subjected to FRAP analysis on a Zeiss 710 inverted confocal microscope. Cells from three independent biological replicates were analyzed and the pooled data used for graphical representation and subsequent statistical analysis. See the supplementary Materials and Methods for details.

### Image analysis for growth cone and filopodial parameters

For both fixed and live imaged growth cones, finger-like projections from the growth cone periphery that were  $\geq 2 \mu\text{m}$  in length were considered as filopodia (Fig. S4). All analysis was carried out using ImageJ (NIH). For details of the image analysis see the supplementary Materials and Methods. For fluorescence quantification, all imaging conditions were kept constant between the experimental sets being compared.

### Phalloidin homoFRET measurements in spinal growth cones

Following polarized excitation, the change in the fluorescence anisotropy measures the homoFRET efficiency. Under these conditions, increased homoFRET indicates higher order compaction as reported by a reduction in fluorescence anisotropy (Chan et al., 2011; Ganguly et al., 2011; Iyer et al., 2012; Tramier and Coppey-Moisan, 2008).

Morpholino-treated growth cones were fixed and stained with 20 units of phalloidin-Alexa Fluor 488 (Invitrogen) as above. The parallel and perpendicular emission components were collected using a PlanApo 63 $\times$ /1.4 on a Zeiss LSM 710 confocal system equipped with an anisotropy module. Images were processed by applying the standard anisotropy equation:  $D = [(S1 - G \times S2) / (S1 + 2G \times S2)] \times 255$ , where D is the anisotropy value, S1 and S2 are the parallel and perpendicular components of emission, respectively, and G is the grating factor for the imaging system which is used to correct any bias towards a particular emission component. To scale the output image to an 8-bit image a factor of 255 is incorporated in the equation. The grating factor was calculated using 1 mM FITC solution in water and was found to be 0.98. All the mathematical transformations were performed using 64-bit Zen 2012 Black edition (Zeiss). The anisotropy image so obtained was imported into ImageJ and a 2 $\times$ 2 median filter was applied to the entire image. Using the original phalloidin image, an outline of the growth cone was drawn using the polygon tool in ImageJ. This region of interest (ROI) was overlaid on the anisotropy image and the anisotropy values enclosed within this ROI were used for comparison across different treatments. Data were analyzed from three independent biological replicates representing 20 growth cones for each treatment. The ImageJ heatmap plugin was used to represent the output images.

### Open-book preparations and quantification of axonal tracts

Following morpholino electroporation (at HH14) and subsequent incubation, the embryos were harvested at HH26 and dissected as described previously (Avraham et al., 2010). The region of the spinal cord between the developing fore and hind limbs was used for analysis. The tissue was fixed in 4% formaldehyde for 30 min and mounted in 1 $\times$  PBS for imaging. The entire depth of the sample was imaged as a z-stack using a PlanApo 20 $\times$ /0.8 water-immersion objective on a Zeiss LSM 780 confocal system in the tiling mode. Analysis of spinal commissural axon tracts is described in the supplementary Materials and Methods. Each embryo was considered an independent biological replicate.

### Figure preparation, graphical representations and statistical analysis

Raw images were processed as described in the supplementary Materials and Methods. All the raw measurements were imported to GraphPad Prism 5 for graphical representation. The box and whisker plots are represented using the Tukey method. The bottom and top of the box are the first and third quartiles, the whiskers span the lowest datum within the 1.5 interquartile range of the lower quartile and the highest datum within the 1.5 interquartile range of the upper quartile; the outliers are represented separately beyond the whiskers. The number of data points used for graphical representation and subsequent statistical analysis are represented below each treatment in the

graphs. These numbers represent the pooled data from three or more independent biological replicates (exact numbers are indicated in the relevant subsections). All statistical comparisons for box plots were made using the Mann–Whitney test or Kruskal–Wallis test followed by Dunn’s post-test in Prism 5. Bar graphs show mean $\pm$ s.e.m. The multiple comparisons were made using one-way ANOVA followed by Dunnett’s post-test.

### Acknowledgements

We acknowledge the help of Dhriti Nagar in preparing the schematics and N. K. Subhedar for critical reading and helpful comments.

### Competing interests

The authors declare no competing or financial interests.

### Author contributions

Conceptualization: A.G. Investigation: A.S., K.G., S.M. and A.J. Writing: A.S. and A.G. Funding acquisition: A.G.

### Funding

Department of Biotechnology, Government of India [BT/PR12698/BRB/10/717/2009] and Nano Mission Council, Department of Science and Technology [SR/NM/NS-42/2009] grants to A.G. and intramural funding from IISER Pune supported this work. Fellowships from the Council of Scientific and Industrial Research (CSIR) and INSPIRE supported A.S. and A.J., respectively.

### Supplementary information

Supplementary information available online at <http://dev.biologists.org/lookup/suppl/doi:10.1242/dev.130104/-/DC1>

### References

- Avraham, O., Zisman, S., Hadas, Y., Vald, L. and Klar, A. (2010). Deciphering axonal pathways of genetically defined groups of neurons in the chick neural tube utilizing in ovo electroporation. *J. Vis. Exp.* **39**, e1792.
- Baeriswyl, T. and Stoeckli, E. T. (2008). Axonin-1/TAG-1 is required for pathfinding of granule cell axons in the developing cerebellum. *Neural Dev.* **3**, 7.
- Baeriswyl, T., Mauti, O. and Stoeckli, E. T. (2008). Temporal control of gene silencing by in ovo electroporation. *Methods Mol. Biol.* **442**, 231–244.
- Bentley, D. and Toroian-Raymond, A. (1986). Disoriented pathfinding by pioneer neurone growth cones deprived of filopodia by cytochalasin treatment. *Nature* **323**, 712–715.
- Berginski, M. E., Vitriol, E. A., Hahn, K. M. and Gomez, S. M. (2011). High-resolution quantification of focal adhesion spatiotemporal dynamics in living cells. *PLoS ONE* **6**, e22025.
- Block, J., Stradal, T.E.B., Hänisch, J., Geffers, R., Köstler, S.A., Urban, E., Small, J.V., Rottner, K. and Faix J. (2008). Filopodia formation induced by active mDia2/Drf3. *J. Microsc.* **231**, 506–517.
- Block, J., Breitsprecher, D., Kühn, S., Winterhoff, M., Kage, F., Geffers, R., Duwe, P., Rohn, J. L., Baum, B., Brakebusch, C. et al. (2012). FMNL2 drives actin-based protrusion and migration downstream of Cdc42. *Curr. Biol.* **22**, 1005–1012.
- Bohner, K. A., Willet, A. H., Kovar, D. R. and Gould, K. L. (2013). Formin-based control of the actin cytoskeleton during cytokinesis. *Biochem. Soc. Trans.* **41**, 1750–1754.
- Bor, B., Vizcarra, C. L., Phillips, M. L. and Quinlan, M. E. (2012). Autoinhibition of the formin Cappuccino in the absence of canonical autoinhibitory domains. *Mol. Biol. Cell* **23**, 3801–3813.
- Bornschiögl, T. (2013). How filopodia pull: what we know about the mechanics and dynamics of filopodia. *Cytoskeleton* **70**, 590–603.
- Bornschiögl, T., Romero, S., Vestergaard, C. L., Joanny, J.-F., Van Nhieu, G. T. and Bassereau, P. (2013). Filopodial retraction force is generated by cortical actin dynamics and controlled by reversible tethering at the tip. *Proc. Natl. Acad. Sci. USA* **110**, 18928–18933.
- Burridge, K. and Wittchen, E. S. (2013). The tension mounts: stress fibers as force-generating mechanotransducers. *J. Cell Biol.* **200**, 9–19.
- Chacón, M. R., Navarro, A. I., Cuesto, G., del Pino, I., Scott, R., Morales, M. and Rico, B. (2012). Focal adhesion kinase regulates actin nucleation and neuronal filopodia formation during axonal growth. *Development* **139**, 3200–3210.
- Chan, C. E. and Odde, D. J. (2008). Traction dynamics of filopodia on compliant substrates. *Science* **322**, 1687–1691.
- Chan, F. T. S., Kaminski, C. F. and Kaminski Schierle, G. S. (2011). HomoFRET fluorescence anisotropy imaging as a tool to study molecular self-assembly in live cells. *ChemPhysChem* **12**, 500–509.
- Chang, C.-W. and Kumar, S. (2013). Vinculin tension distributions of individual stress fibers within cell–matrix adhesions. *J. Cell Sci.* **126**, 3021–3030.

- Charfi, C., Voisin, V., Levros, L.-C., Edouard, E. and Rassart, E. (2011). Gene profiling of Graffi murine leukemia virus-induced lymphoid leukemias: identification of leukemia markers and Fmn2 as a potential oncogene. *Blood* **117**, 1899-1910.
- Chesarone, M. A. and Goode, B. L. (2009). Actin nucleation and elongation factors: mechanisms and interplay. *Curr. Opin. Cell Biol.* **21**, 28-37.
- Colombelli, J., Besser, A., Kress, H., Reynaud, E. G., Girard, P., Caussinus, E., Haselmann, U., Small, J. V., Schwarz, U. S. and Stelzer, E. H. K. (2009). Mechanosensing in actin stress fibers revealed by a close correlation between force and protein localization. *J. Cell Sci.* **122**, 1928-1928.
- Dennerll, T. J., Lamoureux, P., Buxbaum, R. E. and Heidemann, S. R. (1989). The cyto mechanics of axonal elongation and retraction. *J. Cell Biol.* **109**, 3073-3083.
- Dent, E. W., Kwiatkowski, A. V., Mebane, L. M., Philippar, U., Barzik, M., Rubinson, D. A., Gupton, S., Van Veen, J. E., Furman, C., Zhang, J. et al. (2007). Filopodia are required for cortical neurite initiation. *Nat. Cell Biol.* **9**, 1347-1359.
- Esue, O., Harris, E. S., Higgs, H. N. and Wirtz, D. (2008). The filamentous actin cross-linking/bundling activity of mammalian formins. *J. Mol. Biol.* **384**, 324-334.
- Fitzli, D., Stoeckli, E. T., Kunz, S., Siribour, K., Rader, C., Kunz, B., Kozlov, S. V., Buchstaller, A., Lane, R. P., Suter, D. M. et al. (2000). A direct interaction of axonin-1 with NgCAM-related cell adhesion molecule (NrcAM) results in guidance, but not growth of commissural axons. *J. Cell Biol.* **149**, 951-968.
- Ganguly, S., Clayton, A. H. A. and Chattopadhyay, A. (2011). Organization of higher-order oligomers of the serotonin1A receptor explored utilizing homo-FRET in live cells. *Biophys. J.* **100**, 361-368.
- Goh, W. I. and Ahmed, S. (2012). mDia1-3 in mammalian filopodia. *Commun. Integr. Biol.* **5**, 340-344.
- Gomez, T. M. and Letourneau, P. C. (1994). Filopodia initiate choices made by sensory neuron growth cones at laminin/fibronectin borders in vitro. *J. Neurosci.* **14**, 5959-5972.
- Gomez, T. M., Roche, F. K. and Letourneau, P. C. (1996). Chick sensory neuronal growth cones distinguish fibronectin from laminin by making substratum contacts that resemble focal contacts. *J. Neurobiol.* **29**, 18-34.
- Gomez, T. M., Robles, E., Poo, M.-m. and Spitzer, N. C. (2001). Filopodial calcium transients promote substrate-dependent growth cone turning. *Science* **291**, 1983-1987.
- Grabham, P. W. and Goldberg, D. J. (1997). Nerve growth factor stimulates the accumulation of beta1 integrin at the tips of filopodia in the growth cones of sympathetic neurons. *J. Neurosci.* **17**, 5455-5465.
- Gupton, S. L. and Gertler, F. B. (2007). Filopodia: the fingers that do the walking. *Sci. STKE* **2007**, re5.
- Harris, E. S., Rouiller, I., Hanein, D. and Higgs, H. N. (2006). Mechanistic differences in actin bundling activity of two mammalian formins, FRL1 and mDia2. *J. Biol. Chem.* **281**, 14383-14392.
- Heckman, C. A. and Plummer, H. K. (2013). Filopodia as sensors. *Cell. Signal.* **25**, 2298-2311.
- Hoffmann, B. and Schäfer, C. (2010). Filopodial focal complexes direct adhesion and force generation towards filopodia outgrowth. *Cell Adh. Migr.* **4**, 190-193.
- Iyer, K. V., Pulford, S., Mogilner, A. and Shivashankar, G. V. (2012). Mechanical activation of cells induces chromatin remodeling preceding MKL nuclear transport. *Biophys. J.* **103**, 1416-1428.
- Jaiswal, R., Breitsprecher, D., Collins, A., Corrêa, I. R., Jr., Xu, M.-Q. and Goode, B. L. (2013). The formin Daam1 and Fascin directly collaborate to promote filopodia formation. *Curr. Biol.* **23**, 1373-1379.
- Kuo, J.-C., Han, X., Hsiao, C.-T., Yates, J. R., III and Waterman, C. M. (2011). Analysis of the myosin-II-responsive focal adhesion proteome reveals a role for  $\beta$ -Pix in negative regulation of focal adhesion maturation. *Nat. Cell Biol.* **13**, 383-393.
- Law, R., Dixon-Salazar, T., Jerber, J., Cai, N., Abbasi, A. A., Zaki, M. S., Mittal, K., Gabriel, S. B., Rafiq, M. A., Khan, V. et al. (2014). Biallelic truncating mutations in FMN2, encoding the actin-regulatory protein formin 2, cause nonsyndromic autosomal-recessive intellectual disability. *Am. J. Hum. Genet.* **95**, 721-728.
- Leader, B. and Leder, P. (2000). Formin-2, a novel formin homology protein of the cappuccino subfamily, is highly expressed in the developing and adult central nervous system. *Mech. Dev.* **93**, 221-231.
- Leader, B., Lim, H., Carabatsos, M. J., Harrington, A., Ecsedy, J., Pellman, D., Maas, R. and Leder, P. (2002). Formin-2, polyploidy, hypofertility and positioning of the meiotic spindle in mouse oocytes. *Nat. Cell Biol.* **4**, 921-928.
- Leijnse, N., Oddershede, L. B. and Bendix, P. M. (2015). Helical buckling of actin inside filopodia generates traction. *Proc. Natl. Acad. Sci. USA* **112**, 136-141.
- Lundquist, E. A. (2009). The finer points of filopodia. *PLoS Biol.* **7**, e1000142.
- Lynch, J., Meehan, M. H., Crean, J., Copeland, J., Stallings, R. L. and Bray, I. M. (2013). Metastasis suppressor microRNA-335 targets the formin family of actin nucleators. *PLoS ONE* **8**, e78428.
- Machaidze, G., Sokoll, A., Shimada, A., Lustig, A., Mazur, A., Wittinghofer, A., Aebi, U. and Mannherz, H. G. (2010). Actin filament bundling and different nucleating effects of mouse Diaphanous-related formin FH2 domains on actin/ADF and actin/cofilin complexes. *J. Mol. Biol.* **403**, 529-545.
- Mallavarapu, A. and Mitchison, T. (1999). Regulated actin cytoskeleton assembly at filopodium tips controls their extension and retraction. *J. Cell Biol.* **146**, 1097-1106.
- Mattila, P. K. and Lappalainen, P. (2008). Filopodia: molecular architecture and cellular functions. *Nat. Rev. Mol. Cell Biol.* **9**, 446-454.
- Mellor, H. (2010). The role of formins in filopodia formation. *Biochim. Biophys. Acta* **1803**, 191-200.
- Mitchison, T. and Kirschner, M. (1988). Cytoskeletal dynamics and nerve growth. *Neuron* **1**, 761-772.
- Moore, S. W., Biais, N. and Sheetz, M. P. (2009). Traction on immobilized Netrin-1 is sufficient to reorient axons. *Science* **325**, 166.
- Moore, S. W., Zhang, X., Lynch, C. D. and Sheetz, M. P. (2012). Netrin-1 attracts axons through FAK-dependent mechanotransduction. *J. Neurosci.* **32**, 11574-11585.
- Mozhui, K., Ciobanu, D. C., Schikorski, T., Wang, X., Lu, L. and Williams, R. W. (2008). Dissection of a QTL hotspot on mouse distal chromosome 1 that modulates neurobehavioral phenotypes and gene expression. *PLoS Genet.* **4**, e1000260.
- Myers, J. P. and Gomez, T. M. (2011). Focal adhesion kinase promotes integrin adhesion dynamics necessary for chemotropic turning of nerve growth cones. *J. Neurosci.* **31**, 13585-13595.
- Oakes, P. W., Beckham, Y., Stricker, J. and Gardel, M. L. (2012). Tension is required but not sufficient for focal adhesion maturation without a stress fiber template. *J. Cell Biol.* **196**, 363-374.
- Peleg, S., Sananbenesi, F., Zovoilis, A., Burkhardt, S., Bahari-Javan, S., Agis-Balboa, R. C., Cota, P., Wittnam, J. L., Gogol-Doering, A., Opitz, L. et al. (2010). Altered histone acetylation is associated with age-dependent memory impairment in mice. *Science* **328**, 753-756.
- Robles, E. and Gomez, T. M. (2006). Focal adhesion kinase signaling at sites of integrin-mediated adhesion controls axon pathfinding. *Nat. Neurosci.* **9**, 1274-1283.
- Romero, S., Quatela, A., Borschlogl, T., Guadagnini, S., Bassereau, P. and Tran Van Nhiu, G. (2013). Filopodium retraction is controlled by adhesion to its tip. *J. Cell Sci.* **125**, 5587-5587.
- Rosales-Nieves, A. E., Johndrow, J. E., Keller, L. C., Magie, C. R., Pinto-Santini, D. M. and Parkhurst, S. M. (2006). Coordination of microtubule and microfilament dynamics by Drosophila Rho1, Spire and Cappuccino. *Nat. Cell Biol.* **8**, 367-376.
- Schirenbeck, A., Bretschneider, T., Arasada, R., Schleicher, M. and Faix, J. (2005). The Diaphanous-related formin dDia2 is required for the formation and maintenance of filopodia. *Nat. Cell Biol.* **7**, 619-625.
- Schönichen, A., Mannherz, H. G., Behrmann, E., Mazur, A. J., Silvan, U., Schoenenberger, C.-A., Fackler, O. T., Raunser, S., Dehmelt, L. and Geyer, M. (2013). FHOD1 is a combined actin filament capping and bundling factor that selectively associates with actin arcs and stress fibers. *J. Cell Sci.* **126**, 1891-1901.
- Schuh, M. (2011). An actin-dependent mechanism for long-range vesicle transport. *Nat. Cell Biol.* **13**, 1431-1436.
- Schuh, M. and Ellenberg, J. (2008). A new model for asymmetric spindle positioning in mouse oocytes. *Curr. Biol.* **18**, 1986-1992.
- Skau, C. T., Plotnikov, S. V., Doyle, A. D. and Waterman, C. M. (2015). Inverted formin 2 in focal adhesions promotes dorsal stress fiber and fibrillar adhesion formation to drive extracellular matrix assembly. *Proc. Natl. Acad. Sci. USA* **112**, E2447-E2456.
- Stoeckli, E. T. and Landmesser, L. T. (1995). Axonin-1, Nrc-CAM, and Ng-CAM play different roles in the in vivo guidance of chick commissural neurons. *Neuron* **14**, 1165-1179.
- Tramier, M. and Copepy-Moisan, M. (2008). Fluorescence anisotropy imaging microscopy for homo-FRET in living cells. *Methods Cell Biol.* **85**, 395-414.
- Vizcarra, C. L., Bor, B. and Quinlan, M. E. (2014). The role of formin tails in actin nucleation, processive elongation, and filament bundling. *J. Biol. Chem.* **289**, 30602-30613.
- Walcott, S. and Sun, S. X. (2010). A mechanical model of actin stress fiber formation and substrate elasticity sensing in adherent cells. *Proc. Natl. Acad. Sci. USA* **107**, 7757-7762.
- Yaginuma, H., Shiga, T. and Oppenheim, R. W. (1994). Early developmental patterns and mechanisms of axonal guidance of spinal interneurons in the chick embryo spinal cord. *Prog. Neurobiol.* **44**, 249-278.

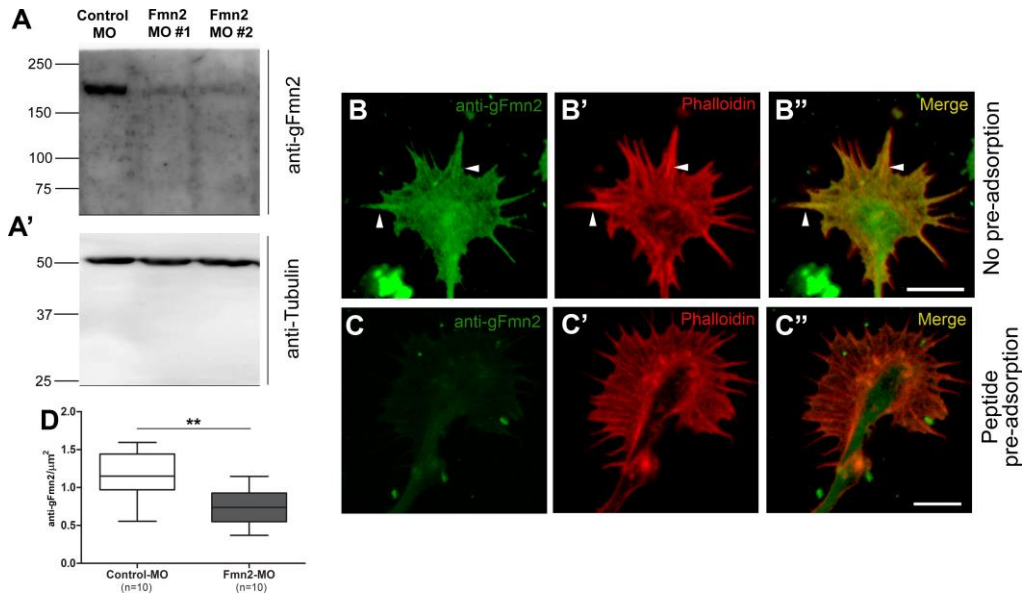


**Figure S1: Specificity of anti-gFmn2 antibody.**

(A and A') Western blot along with loading control showing the detection of a single band in the expected range of molecular weight by the anti-gFmn2 antisera and its reduction upon treatment by Fmn2 morpholinos.

(B-B'') Immunofluorescence for gFmn2 using anti-gFmn2 antisera on spinal growth cones. Fmn2 localization along the filopodial actin bundles can be seen (Arrowheads).

(C-C'') Immunofluorescence for gFmn2 using peptide pre-adsorbed anti-gFmn2 antisera on spinal growth cones. The characteristic pattern of Fmn2 localization along filopodial actin bundles is no more evident. In addition, the overall intensity of the signal is reduced. Images captured under identical conditions as B-B''.

(D) Quantification for anti-gFmn2 immunofluorescence normalized to the growth cone area. The overall signal is reduced upon Fmn2-MO treatment. Data represented as box and whisker plot using Tukey's method. (\*,  $p < 0.05$ )

(Scale Bar  $10\mu\text{m}$ )

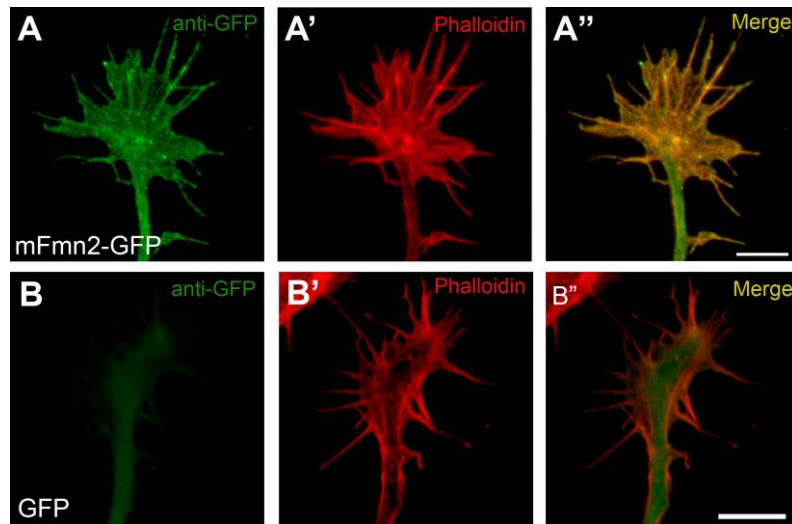


**Figure S2: gFmn2 signal post-permeabilization.**

(A-A'') anti-GFP immunofluorescence for mFmn2-GFP transfected growth cone following brief permeabilization of the growth cone before fixation. Fmn2 can be seen along the filopodial actin bundles.

(B-B'') anti-GFP immunofluorescence for GFP transfected growth cone following brief permeabilization of the growth cone before fixation. The signal is considerably reduced overall and along filopodia.

(Scale bar 10 $\mu$ m in all images)

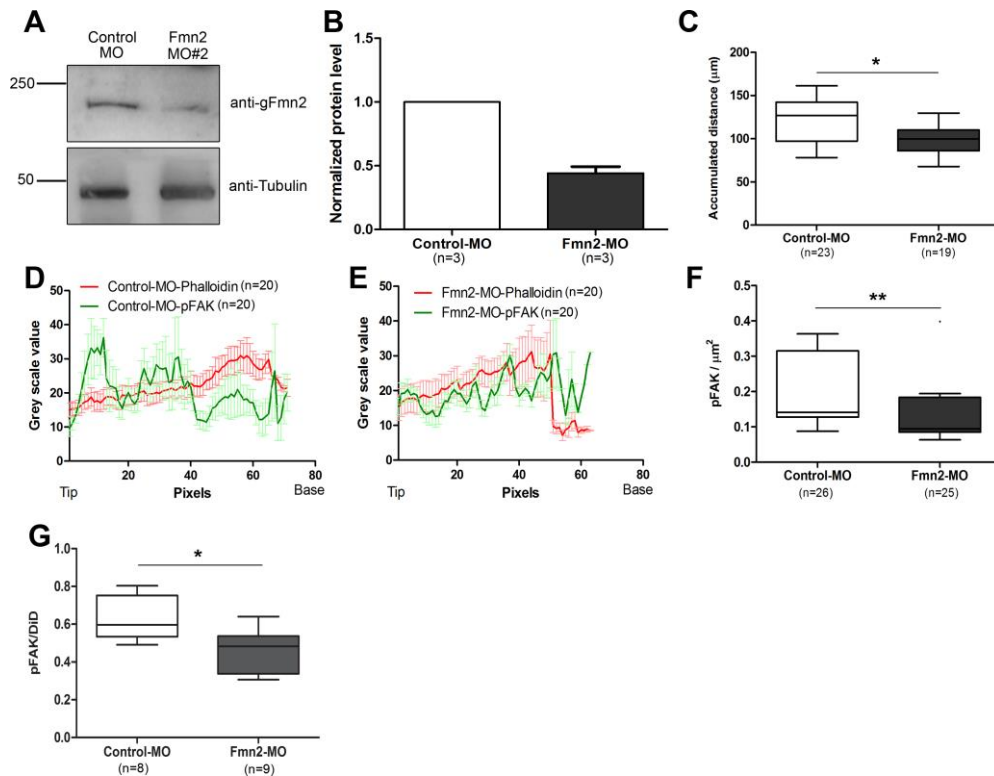


**Figure S3: Effect of Fmn2 knockdown in spinal growth cones *in vitro*.**

(A) Western blot showing reduction in Fmn2 protein level in cultured primary neurons 48 hours after morpholino electroporation.

(B) Densitometric quantification of western blots showing reduction in Fmn2 protein levels post morpholino treatment. Columns represent the mean and the error bars indicate SEM.

(C) Comparison of the total distance (accumulated distance) covered by spinal growth cones in cultures following the morpholino treatments.

(D) pFAK and phalloidin intensities from line traces along filopodia in control morpholino treated growth cones. Data is pooled over 20 individual filopodia from more than three independent experiments. The line represents the mean and the error bars represent SEM.

(E) pFAK and phalloidin intensities from line traces along filopodia in Fmn2 morphant growth cones. Data is pooled over 20 individual filopodia from more than three independent experiments. The line represents the mean and the error bars represent SEM.

(F) Quantification of pFAK (Y-397) intensity in the entire growth cone, normalized to the growth cone area.

(G) pFAK signal normalized to the membrane signal (DiD staining) post morpholino treatment. The drop in this ratio is consistent with the earlier observation of reduced anti-gFmn2 signal in Fmn2-MO treated growth cones.

(Data in C, F and G are represented as box and whisker plots using the Tukey method. The horizontal line inside the box represents the median. Statistical comparisons were done using the Mann-Whitney test; \*,  $p \leq 0.05$ , \*\*,  $p \leq 0.01$ )

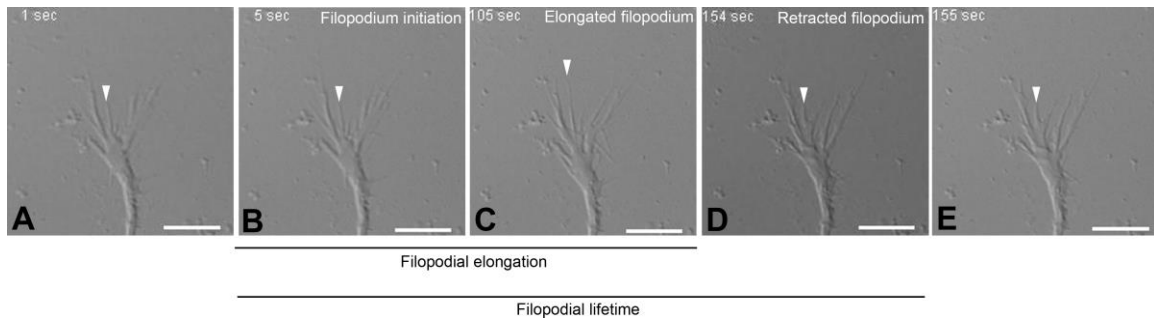


### Figure S4: Analysis of filopodial dynamics.

Snapshots from a representative time lapse movie used for analyzing filopodial dynamics. Arrowhead marks the filopodia analyzed. Thin finger-like projection at the leading edge of the growth cone greater than  $2\mu\text{m}$  was considered as a filopodium.

(A) Marked protrusion is less than  $2\mu\text{m}$ .

(B) Protrusion marked in A grows to  $2\mu\text{m}$  and is included in the analysis. This is categorized as an initiation event.

(C) The same protrusion is followed over time for elongation and retraction. The rate of increase in length from B to C is the elongation rate.

(D) Filopodium being tracked retracts to  $2\mu\text{m}$ . The time between B and D is considered as the filopodial lifetime.

(E) Filopodium being tracked falls below the  $2\mu\text{m}$  cut-off.

(Scale bar  $10\mu\text{m}$  in all images)

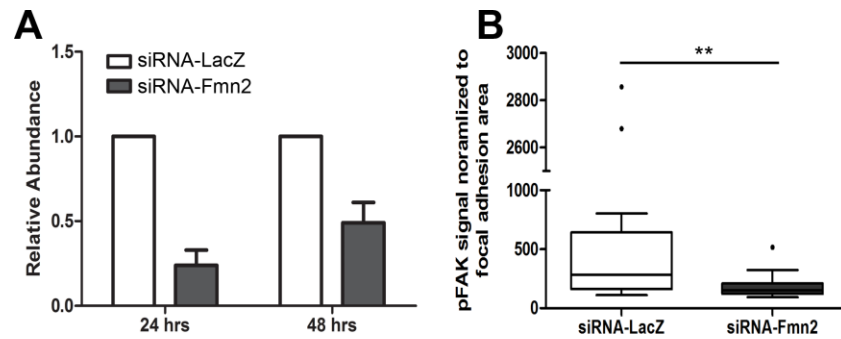


**Figure S5: siRNA mediated knockdown of Fmn2 and reduction of pFAK in NIH3T3 fibroblasts.**

(A) qRT-PCR quantification for the relative transcript levels of Fmn2 after siRNA mediated knockdown in NIH3T3 cells. Columns represent the mean and the error bars indicate SEM.

(B) Comparison of the pFAK intensities at focal adhesions normalized to the focal adhesion area in control and Fmn2 siRNA treated cells. Data are represented as box and whisker plots using the Tukey method. The horizontal line inside the box represents the median. Statistical comparisons were done using the Mann-Whitney test; \*\*,  $p \leq 0.01$ .

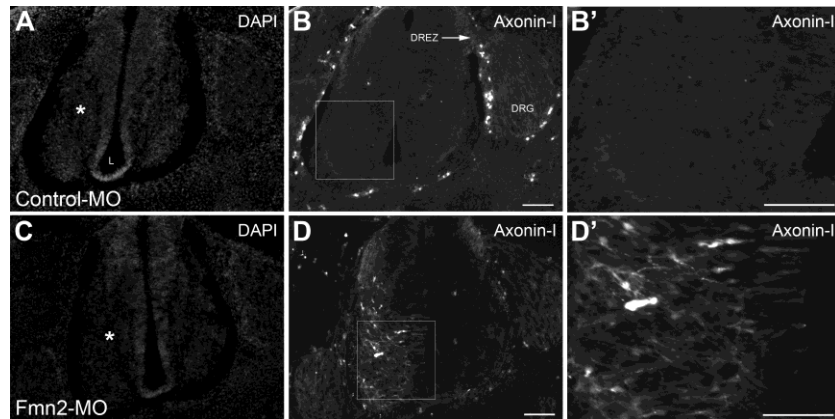


**Figure S6: Aberrant Axonin-I expression in Fmn2 morphant spinal cords.**

Representative micrographs of cryosections from whole embryos (Stage HH26) immunostained for Axonin-I. L: spinal cord lumen, DRG: Dorsal root ganglion, DREZ: Dorsal root entry zone. The asterisk marks the side receiving the morpholino.

(A) Control morpholino treated spinal cord showing DAPI stained nuclei.

(B) Axonin-I staining pattern for the cryosection in A. Axonin-I signal is restricted to the DRG and DREZ at this stage.

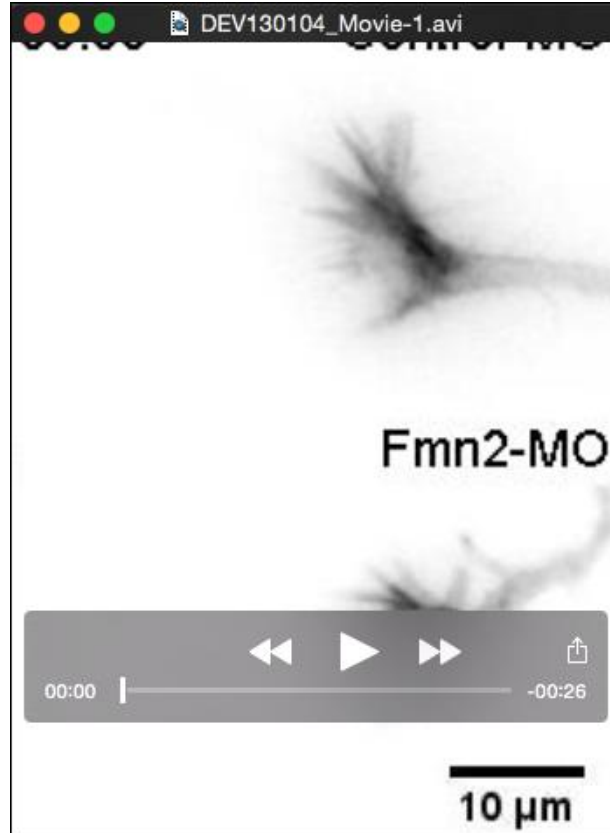
(B') Enlarged view of the marked region in B showing absence of Axonin-I positive axonal tracts.

(C) Fmn2 morpholino treated spinal cord showing DAPI stained nuclei.

(D) Axonin-I staining pattern for the cryosection in A. In addition to the DRG and DREZ, Axonin-I expressing axonal tracts were visible only on the side receiving the Fmn2 morpholino.

(D') Enlarged view of the boxed region in B showing the presence of Axonin-I positive axonal tracts.

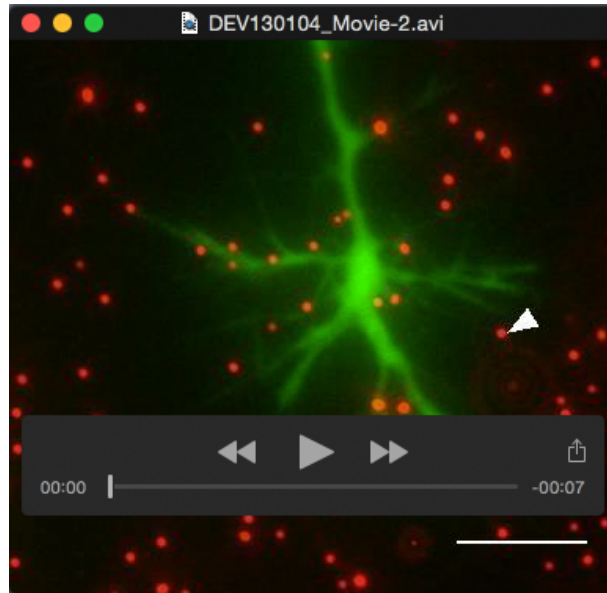
(Scale bar, 100µm in B and D; 50µm in B", D")



**Movie 1: Growth cone translocation.**

Morpholino treated growth cones were imaged live to assess the motility parameters.

Fmn2-MO treated growth cones failed to advance as efficiently as the Control-MO treated growth cones. (Scale Bar, 10μm)



**Movie 2: Analysis of traction generation by growth cone filopodia.**

Transfected growth cones (green) were plated compliant gels embedded with fluorescent beads (red) and imaged live. Movement of the beads at the filopodial tip was analyzed (arrowhead). (Scale Bar 10 $\mu$ m)

## **Supplementary Materials and Methods**

### ***In ovo* electroporations**

Embryos at stage HH14 were used for electroporations. Spinal cord electroporations were done similar to the procedure described earlier (Baeriswyl et al., 2008). Briefly, 5 pulses of 20V were delivered where each pulse lasted for 50ms with an inter-pulse interval of 100ms. All the morpholinos were used at 750 $\mu$ M and plasmids were used between 1 $\mu$ g/ $\mu$ l to 1.5 $\mu$ g/ $\mu$ l. CUY21SC (Nepagene) square wave electroporator was used to electroporate.

### **Cloning of pCAG-mFmn2-GFP and Atoh1-mFmn2**

The original clone for mFmn2 was obtained from Prof. Philip Leder and sub-cloned in to pCAG-GFP vector using Kpn1 and Xma1 sites (Forward primer- ATGGGGAACCAGGATGGGAAG, reverse primer- CGTTTTTCATGCTTATCTTCGCTTTAATC). The Atoh1 enhancer was isolated from the parent plasmid using PCR (Forward primer- ACCTGGTCGACTCCAAGGTCCGGCAATGAAG, Reverse primer- GTACCGTCGACGCAGGCTAGAAGCAAATGTAAGC) and cloned in to pCAG-mFmn2-GFP to replace the CAG enhancer.

### **Immunostaining and imaging of cultured primary neurons**

Post electroporations, the cell suspension was plated on poly-L-lysine (1mg/ml) and fibronectin (50 $\mu$ g/ml) coated cover glass bottom dishes with culture medium (L-15+10%

heat inactivated FBS+1x Pen-Strep+2mM L-glutamine) and incubated at 37°C without CO<sub>2</sub> for 48 hours.

Standard fixation (4% paraformaldehyde and 0.05% glutaraldehyde in 1x PBS) and permeabilization (0.01% TritonX-100 in 1x PBS) procedures were followed during immunostaining. For the anti-GFP staining, the growth cones were briefly permeabilized (138nM KCl, 10mM PIPES, 3mM EGTA, 4mM MgCl<sub>2</sub>, 1% BSA, 0.025% saponin and 0.1mM ATP, pH 6.9) before fixation. Anti-gFmn2 antiserum (generated as described earlier) was used at 1:200, while all other primary antibodies (anti-GFP, AbCam, ab290; anti-pFAK-Y397, AbCam, ab4803) were used at 1:1000 dilutions. Corresponding secondary antibodies (Invitrogen) were used at 1:1000 dilutions. Fluorescently labeled phalloidin (Invitrogen) was used at 1:1000 dilution. For the membrane labeling experiments using DiD, the samples were incubated with 10µM DiD solution (Invitrogen) for 30 minutes followed by three washes with 1x PBS, 10 minute each. After staining, the samples were stored and imaged in 1x PBS. Imaging was done using a PlanApo 63x/1.4 objective on a Zeiss 710 inverted confocal system using appropriate laser lines. Growth cones from three independent biological replicates were analyzed and the pooled data was used for graphical representation and statistical analysis.

### **Validation of the custom raised gFmn2 antibody**

The electroporated halves of spinal cords between the fore- and hind limbs from five individual embryos were collected 48 hours post electroporation (Stage HH26) and protein lysates were prepared using the RIPA buffer. 20µg protein from each of the samples was used for SDS-PAGE and standard western blotting procedure was

followed. Total anti-serum from the 6th bleed was used to probe gFmn2 on the blots. Anti-tubulin (DM1A, Sigma) antibody was used for loading controls.

*Peptide pre-adsorption:* The anti-Fmn2 antiserum was pre-incubated with 10 $\mu$ g peptide for 3 hours at 4°C and then used for immunostaining of the spinal growth cones as described later. Data from two independent biological replicates were used for graphical representation and statistical analysis.

### **Image analysis for growth cone and filopodial parameters**

The phalloidin stained outline of the growth cones was manually traced using the polygon selection tool in ImageJ to measure the area of the growth cone. Finger like projections from the growth cone periphery equal to or longer than 2 $\mu$ m was considered as a filopodium. The number of filopodia per growth cone was manually counted and the lengths of filopodia were measured using the line tool in ImageJ. Data from five independent biological replicates were analyzed and the pooled data was used for graphical representation and subsequent statistical analysis. For the rescue experiments, 10 $\mu$ g pCAG-Fmn2-GFP was co-transfected along with the morpholinos as described earlier. Three independent biological replicates were used for graphical representation and statistical analysis.

The center of the growth cone was tracked across the time series using the manual tracker plugin in ImageJ and the co-ordinates were exported to the Chemotaxis and Migration tool developed by Ibidi (<http://ibidi.com/xtproducts/en/Software-and-Image-Analysis/Manual-Image-Analysis/Chemotaxis-and-Migration-Tool>). The speed, accumulated distance, displacement and directionality were measured using the

Chemotaxis and Migration tool. Data from five independent biological replicates were analyzed and the pooled data was used for graphical representation and subsequent statistical analysis.

For analysis of filopodial initiation, elongation rates and lifetimes, the growth cones were transfected and cultured as described earlier on fibronectin coated cover glass bottom chambers. Differential Interference Contrast (DIC) images were acquired at 1 second intervals for 10 minutes using a PlanApo 60x/1.4 objective on an Olympus IX81 system equipped with a Hamamatsu ORCA-R<sup>2</sup> CCD camera. Individual filopodia were cropped and a montage was made for the entire time lapse in Image J. Protrusions equal to or longer than 2 $\mu$ m were considered as filopodia. Any fingerlike protrusion smaller than 2 $\mu$ m that elongated to or beyond 2 $\mu$ m during the imaging period was considered as a filopodial initiation event. The filopodial tip was tracked manually in each frame till it achieved the maximum length and the elongation rate was subsequently calculated for each of these events. Time for which any filopodium remained above the 2 $\mu$ m threshold was considered as the filopodial lifetime (Figure S4). Data from four independent biological replicates representing 30 (Control-MO) and three independent biological replicates representing 22 (Fmn2-MO) growth cones were analyzed and the pooled data used for graphical representation and subsequent statistical analysis.

Line traces for the pFAK analysis were done using the line tool in Image J. The phalloidin channel was used as a reference to identify the filopodia. 2 pixel wide line was drawn manually along the filopodial actin bundle on the phalloidin channel and the ROI was transferred to the pFAK channel. Intensity measurements were done using Image J and the raw values were exported to GraphPad Prism 5 for graphical

representation and statistical analysis. Data from three individual biological replicates were analyzed and the pooled data used for graphical representation and subsequent statistical analysis.

### **Filopodial traction assay**

Filopodial traction force assays were modified from an earlier protocol (Chan and Odde, 2008). Briefly, 1.1 kPa polyacrylamide gels were prepared on cover glasses as described earlier by Tse et al. 2010 (Tse and Engler, 2010). 200 nm beads were embedded in the gel during the gel preparation. The gels were treated with sulfo-SANPAH (Thermo Scientific) and UV treated (360nm) for cross linking with fibronectin (50µg/ml, Sigma). Electroporated primary neurons were plated on gels in culture media with 0.6% methocel and 100ng/ml NGF and incubated for 48 hours prior to imaging. Bead pulling events were captured every 3.3 seconds using a PlanApo 100x/1.4 oil immersion objective on an Olympus IX81 system equipped with a Hamamatsu ORCA-R<sup>2</sup> CCD camera. Beads were automatically tracked using a particle tracking algorithm ([http://courses.washington.edu/me333afe/ImageJ\\_tutorial.html](http://courses.washington.edu/me333afe/ImageJ_tutorial.html)) and displacements above the calculated RMS inaccuracy of the algorithm considered for analysis. Two independent biological replicates representing 10 filopodia with 120 events (Control-MO) and 16 filopodia with 117 events (Fmn2-MO) were analyzed.

### **Quantitative RT-PCR for NIH3T3 cells**

Following the siRNA transfection, total RNA isolation procedure was followed using TRIZOL®. cDNA was prepared using 1µg total RNA, oligo-dT (18mer) and M-MLV

reverse transcriptase (Promega) according to the manufacturer's recommendations. Each sample had three technical replicates in an experiment and each experiment was repeated thrice as biological replicates. The pooled data were used for statistical analysis and graphical representations. Normalization for Fmn2 (Forward primer- TCCTCTATTTTGGAAAGCCCG, Reverse primer- TTTGTGCGTAGATCCTCGATG) were done using  $\beta$ -actin (Forward primer- TCACTATTGGCAACGAGCG, Reverse primer- AGGTCTTTACGGATGTCAACG).

### **Quantification of pFAK intensities at the focal adhesions in NIH3T3 fibroblasts**

After the siRNA treatment as described earlier, standard fixation (4% paraformaldehyde and 0.05% glutaraldehyde in 1x PBS) and permeabilization (0.01% TritonX-100 in 1x PBS) procedures were followed during immunostaining. pFAK-Y397 antibody (Dumont et al., 2009) was used at 1:1000 dilution. Corresponding secondary antibodies (Invitrogen) were used at 1:1000 dilution.

Imaging was done using a PlanApo 63x/1.4 objective on a Zeiss 710 inverted confocal system using appropriate laser lines. The Paxillin channel was used to create a mask of the focal adhesions using the FAAS (<http://faas.bme.unc.edu/>; Berginski et al., 2011). This mask was transferred to the pFAK channel and the pFAK intensities were recorded through this mask to obtain signal intensities specifically for the focal adhesions. For each cell, the pFAK intensities thus obtained were normalized with the total focal adhesion area and the raw values were exported to GraphPad Prism 5 for graphical representation and statistical analysis. Data from three independent biological replicates were pooled for statistical analysis and graphical representation.

### **Focal adhesion analysis in NIH3T3 fibroblasts**

Paxillin-EGFP labeled focal adhesions were imaged in TIRF mode 24 hours post siRNA treatment. The image series were processed through the FAAS (<http://faas.bme.unc.edu/>; Berginski et al., 2011). This analysis used high pass and round averaging filters in combination with water algorithm to segment and identify focal adhesions. Once identified, the focal adhesions were tracked over the entire image sequence. The first image in the time series was used to estimate the number of focal adhesions per cell and focal adhesion size while the entire time series was analyzed for the dynamics parameters like assembly and disassembly kinetics.

### **Ventral stress fiber FRAP analysis**

24 hours post siRNA+mGFP-Actin transfection, the culture medium was replaced with cells imaging medium (L-15+10% heat inactivated FBS+1x Pen-Strep+2mM L-glutamine). Imaging was done using a PlanApo 63x/1.4 objective on a Zeiss 710 inverted confocal system using the 488nm laser line. A 4 x 16 pixel ROI was randomly selected along the ventral stress fibers. Images were acquired every 1 second for 300 seconds. 10 pre-bleach images were acquired at 2% laser power for reference. Bleaching was done using 100% laser power with 50 iterations. Following the bleaching, images were acquired at 2% laser power. The images were analyzed using Image J. Images were first subjected background subtraction. Mean intensity of the bleached region was recorded each frame and corrected for bleaching using the mean intensity for the whole cell. The raw values for the bleached ROI so obtained were imported to

GraphPad Prism 5 and the curve fitting was done using a double exponential fit. Fits were compared using the Extra sum-of-squares F-test.

### **Quantification of pFAK line traces and total pFAK signal in the growth cones**

Line traces for the pFAK analysis were done using the line tool in Image J. The phalloidin channel was used as a reference to identify the filopodia. 2 pixel wide line was drawn manually along the filopodial actin bundle on the phalloidin channel and the ROI was transferred to the pFAK channel. Using the original phalloidin image an outline of the growth cone was drawn using the polygon tool in Image J. This ROI was overlaid on the pFAK image and the intensity values enclosed within this ROI were normalized to the growth cone area used for comparison across different treatments. Intensity measurements were done using Image J and the raw values were exported to GraphPad Prism 5 for graphical representation and statistical analysis.

Comparison for the distal segments of the filopodia was done by normalizing the total signal in the distal half of the filopodium by the total signal in the filopodium.

### **Imaging NIH3T3 fibroblasts**

Post transfection, the cells were fixed (4% paraformaldehyde and 0.05% glutaraldehyde in 1x PBS), followed by washing with PBST. F-actin structures were marked using fluorescently labeled phalloidin. Cells were then stored in 1xPBS till imaging. Images were acquired using a PlanApo 63x/1.4 objective on a Zeiss 800 inverted confocal system using appropriate laser lines.

For live cell imaging, the culture medium was replaced with imaging medium (L-15+10% heat inactivated FBS+1x Pen-Strep+2mM L-glutamine) 48 hours post transfections. Z-stacks were acquired in wide-field mode on Olympus IX81 system (ApoN/TIRF 60x/1.49) equipped with a Hamamatsu ORCA-R<sup>2</sup> CCD camera. The system was equipped with a focus drift correction mechanism and the entire imaging setup was maintained at 37°C without CO<sub>2</sub> during the entire imaging procedure. The images were deconvolved using the Adaptive blind iterative deconvolution feature in the AutoQuantX3 software (MediaCybernetics).

### **Analysis of spinal commissural axonal tracts**

*Pre-crossing/Post-crossing ratio:* Three regions of 100µm length each were randomly selected in the pre crossing area of the spinal open book image (100µm from the floor plate; Figure 8D), with the selector being blind to the treatment and the fate of the post-crossing axons (pre-crossing and post-crossing axons are in different focal planes). Corresponding to pre-crossing, three line ROIs of 100µm length each were selected in the post-crossing area (150µm from the floor plate; Figure 8D). Number of axonal tracts was manually counted in the post-crossing and pre-crossing regions of a maximum intensity projection image. Post to pre-crossing ratio was calculated for the 3 regions and was averaged to get a post to pre-crossing axonal tract number ratio for a spinal cord.

*Evaluation of axonal trajectories:* Three regions of 150µm x 150µm each were randomly selected 50 µm away from the midline in the post crossing area of the spinal open book image, without visualizing the post-crossing axons (pre-crossing and post-crossing

areas are in different focal planes). The post crossing axonal tracts were segregated into categories based on their trajectories. Straight – tracts that moves straight in the contra-lateral side without taking any turn towards the rostral or caudal side (majority of them are seen in focal plane different from other post-crossing axons), Opposite - tracts that take a turn and extend towards the caudal side, Non-sigmoid – tracts that take a sharp turn and extended parallel to the floor plate and Aberrant – contra-lateral tracts displaying no apparent directionality and Sigmoid- tracts that take a distinct sigmoid turn towards the rostral side after crossing the midline. Only the sigmoidal trajectories were analyzed as they were the predominant category. The number of post crossing axons in the box that showed sigmoid trajectories was counted along a diagonal in the box. The number of sigmoidal trajectories was normalized to the total number of axonal trajectories in the region of interest. After normalizing the number of post crossing sigmoidal trajectories individually for all three regions of interest, the values were averaged for a given treatment.

### **Fixation, cryosectioning and immunohistochemistry**

Electroporated embryos were collected at stage HH26 and fixed overnight in 4% paraformaldehyde at 4°C. The embryos were then processed through a sucrose gradient series prepared in 1x PBS (10% overnight, 20% overnight, 30% overnight). Finally the whole embryos were positioned and embedded in OCT® (Tissue-Tek) for cryosectioning. The region between the fore limbs and hind limbs was sectioned at 10µm intervals using a Leica CM1950 cryotome. Standard permeabilization (0.1% TritinX-100 in 1xPBS) and blocking (5% normal goat serum) procedures were followed.

Axonin-I positive commissural neurons were stained using the 23.4-5s antibody (DSHB) at 1:10 dilution. The secondary antibody was used at 1:1000. Sections were mounted in mounting medium (20mM Tris-HCL, pH 8.0 and 0.5% propyl gallate in 90% glycerol). Images were acquired using a PlanApo 20x/0.8 objective on a Zeiss ImagerZ.1 upright fluorescence microscope.

### **Figure preparation**

All raw images were rotated and cropped using Image J and then imported to Photoshop CS3 as RGB layers. Adjustment for brightness/contrast and windows/levels were performed equally between treatments and controls for better visualization. Quantification of fluorescence intensity was performed on unadjusted, raw micrographs. Graphs were exported as TIFF images from GraphPad Prism 5 and subsequently imported to Photoshop CS3, cropped and arranged appropriately.

## Supplementary references

- Baeriswyl, T., Mauti, O. and Stoeckli, E. T.** (2008). Temporal Control of Gene Silencing by in ovo Electroporation. In *Methods in Molecular Biology*, pp. 231–244.
- Chan, C. E. and Odde, D. J.** (2008). Traction dynamics of filopodia on compliant substrates. *Science (80-. )*. **322**, 1687–91.
- Dumont, R. a, Hildebrandt, I., Su, H., Haubner, R., Reischl, G., Czernin, J. G., Mischel, P. S. and Weber, W. a** (2009). Noninvasive imaging of alphaVbeta3 function as a predictor of the antimigratory and antiproliferative effects of dasatinib. *Cancer Res.* **69**, 3173–9.
- Tse, J. R. and Engler, A. J.** (2010). Preparation of hydrogel substrates with tunable mechanical properties. In *Current Protocols in Cell Biology*, pp. 1–16.